Article

TRANSPARENT PROCESS OPEN ACCESS

EMBO reports

RAB6 and dynein drive post-Golgi apical transport to prevent neuronal progenitor delamination

Jean-Baptiste Brault[1], Sabine Bardin[1], Marusa Lampic[1], Jacopo A Carpentieri[1], Laure Coquand[1,2], Maxime Penisson[2,3,4], Hugo Lachuer[1], Guiliana Soraya Victoria[1], Sarah Baloul[1], Fatima El Marjou[1], Gaelle Boncompain[1], Stephanie Miserey-Lenkei[1], Richard Belvindrah[2,3,4], Vincent Fraisier[5], Fiona Francis[2,3,4], Franck Perez[1], Bruno Goud[1,*] & Alexandre D Baffet[1,6,**]

Abstract

Radial glial (RG) cells are the neural stem cells of the developing neocortex. Apical RG (aRG) cells can delaminate to generate basal RG (bRG) cells, a cell type associated with human brain expansion. Here, we report that aRG delamination is regulated by the post-Golgi secretory pathway. Using *in situ* subcellular live imaging, we show that post-Golgi transport of RAB6+ vesicles occurs toward the minus ends of microtubules and depends on dynein. We demonstrate that the apical determinant Crumbs3 (CRB3) is also transported by dynein. Double knockout of RAB6A/A' and RAB6B impairs apical localization of CRB3 and induces a retraction of aRG cell apical process, leading to delamination and ectopic division. These defects are phenocopied by knockout of the dynein activator LIS1. Overall, our results identify a RAB6-dynein-LIS1 complex for Golgi to apical surface transport in aRG cells, and highlights the role of this pathway in the maintenance of neuroepithelial integrity.

Keywords cell polarity; dynein; neocortex development; polarized trafficking; RAB6

Subject Categories Cell Adhesion, Polarity & Cytoskeleton; Membrane & Trafficking; Neuroscience

DOI 10.15252/embr.202254605 | Received 4 January 2022 | Revised 18 July 2022 | Accepted 25 July 2022 | Published online 18 August 2022

EMBO Reports (2022) 23: e54605

Introduction

In the developing neocortex, all neurons derive from neural stem cells called radial glial (RG) progenitor cells(Paridaen & Huttner, 2014; Uzquiano *et al*, 2018). These highly elongated cells also serve as tracks for the migration of newborn neurons into the cortical plate. Two types of RG cells have been identified: apical RG (aRG) cells (also known as vRG cells), located in the ventricular zone (VZ), and basal RG cells (bRG cells, also known as oRG cells) located in the subventricular zone (Fietz *et al*, 2010; Hansen *et al*, 2010; Reillo *et al*, 2011; Fig 1A). aRG cells are common to all mammalian species while bRG cells, which originate from aRG cells, are rare in lissencephalic species such as mice but abundant in gyrencephalic species, including humans (Fernández *et al*, 2016; Florio *et al*, 2016; Penisson *et al*, 2019). aRG cells are tightly connected to each other by adherens junctions and form a pseudostratified epithelium lining the ventricle (Lee & Norden, 2013). They are highly polarized and display an apical process extending to the ventricular surface, and a long basal process, connecting to the pial surface (Fig 1A). Several studies have illustrated that apicobasal polarity is critical for the maintenance of aRG cells, and that its alteration can lead to aRG cell delamination from the neuroepithelium and to the generation of bRG-like cells (Cappello *et al*, 2006; Itoh *et al*, 2013; Johnson *et al*, 2018; Narayanan *et al*, 2018; Tavano *et al*, 2018). In ferrets, the cell adhesion molecule cadherin 1 is downregulated at the critical period of bRG cell generation and its knockdown is sufficient to induce bRG cell generation(Martínez-Martínez *et al*, 2016).

Epithelial polarity is controlled by the PAR, Crumbs, and Scribble complexes which mutually interact to generate and maintain apical and basolateral domains. The Crumbs complex is composed of CRB, PALS1, and PATJ and is a major apical domain determinant (Bulgakova & Knust, 2009). In the mouse developing neocortex, knockout of CRB1 and CRB2 leads to an alteration of aRG cells apical junctions, while knockout of PALS1 causes severe polarity defects, apoptotic cell death, and microcephaly (Kim *et al*, 2010; Dudok *et al*, 2016). The establishment and maintenance of epithelial polarity also rely on polarized trafficking along the biosynthetic/secretory

1 Institut Curie, PSL Research University, CNRS UMR144, Paris, France
2 Sorbonne University, Paris, France
3 INSERM UMR-S 1270, Paris, France
4 Institut du Fer à Moulin, Paris, France
5 UMR 144-Cell and Tissue Imaging Facility (PICT-IBiSA), CNRS-Institut Curie, Paris, France
6 Institut National de la Santé et de la Recherche Médicale (INSERM), Paris, France
*Corresponding author. Tel: +33 1 42 34 63 98; E-mail: bruno.goud@curie.fr
**Corresponding author. Tel: +33 1 56 24 63 68; E-mail: alexandre.baffet@curie.fr

pathway. Newly synthesized transmembrane proteins are sorted in the Golgi apparatus/TGN (*Trans*-Golgi Network) and are routed towards the apical or basolateral domains of epithelial cells, possibly transiting through endosomal compartments (Apodaca *et al*, 2012). In particular, the secretory pathway is essential for the apical targeting of newly synthesized CRB, the only transmembrane protein among the apical polarity complexes (Rodriguez-Boulan & Macara, 2014).

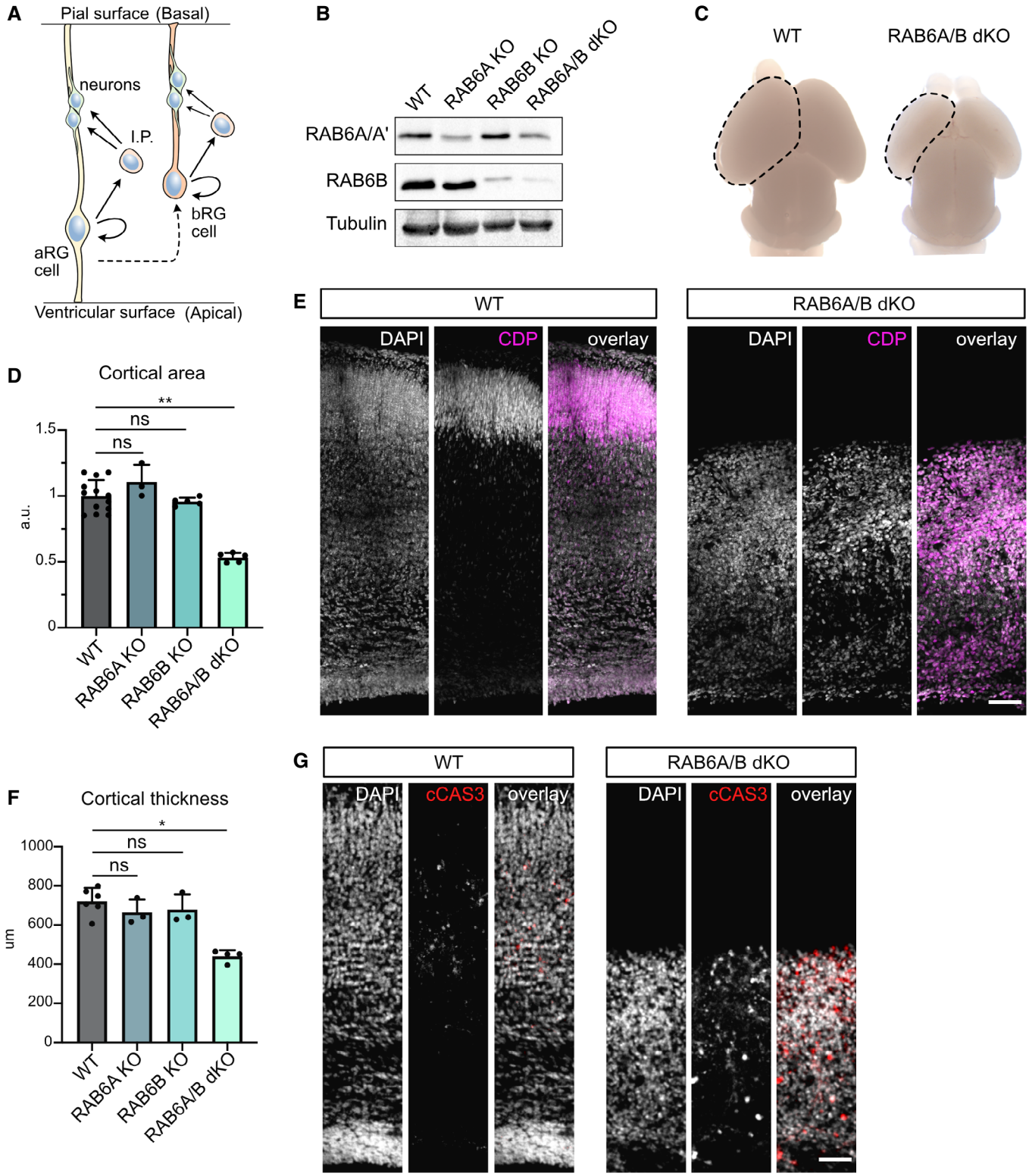

Figure 1.

Figure 1. *RAB6A/B* double knockout causes microcephaly.

A Schematic representation of cortical neurogenesis. Apical radial glial (aRG) cells are epithelial cells and the main neuronal progenitors in mouse. Basal radial glial (bRG) cells are rare in mouse but are the most abundant progenitor population in human. They have delaminated from the neuroepithelium. I.P.: Intermediate Progenitor.

B Western blot analysis of RAB6A/A' and RAB6B protein levels in *WT*, *Emx1-Cre; RAB6*$^{loxP/loxP}$ (*RAB6A* KO), *RAB6B*$^{-/-}$ (*RAB6B* KO) and *Emx1-Cre; RAB6A*$^{loxP/loxP}$; *RAB6B*$^{-/-}$ (*RAB6A/B* dKO) E15.5 cortical extracts.

C P0 WT and *RAB6A/B* dKO brains. A cortical hemisphere is circled (dotted lines).

D Cortical area in WT (N = 13 brains), *RAB6A* KO (N = 3 brains), *RAB6B* KO (N = 5 brains), and *RAB6A/B* dKO (N = 5 brains) at P0.

E WT and *RAB6A/B* dKO brains stained for layer II/III marker CDP at P0. Scale bar = 100 μm.

F Cortical thickness (μm) in WT (N = 6 brains), *RAB6A* KO (N = 3 brains), *RAB6B* KO (N = 3 brains) and *RAB6A/B* dKO (N = 4 brains) at P0.

G Immunostaining for cleaved Caspase 3 (cCAS3) in WT and *RAB6A/B* dKO brains at P0. Scale bar = 50 μm.

Data information: (D, F) Kruskal–Wallis test with a Dunn *post-hoc* test and Benjamini–Hochberg procedure. All error bars indicate SD.

RAB6 is a Golgi/TGN-associated small GTPase which controls both anterograde and retrograde transport, from and toward the Golgi apparatus (Goud *et al*, 2018). Three RAB6 paralogs have been identified: ubiquitous RAB6A (and its splicing variant RAB6A'), RAB6B, predominantly expressed in the brain, and RAB6C, encoded by a primate-specific retrogene and involved in cell cycle progression (Opdam *et al*, 2000; Goud *et al*, 2018). In non-polarized cells, RAB6A is associated with most—if not all—post-Golgi vesicles, irrespective of the transported cargo, suggesting that RAB6A is a general regulator of post-Golgi trafficking (Fourriere *et al*, 2019). The exact role of RAB6B is poorly known but evidence exist that it acts redundantly with RAB6A in the secretory pathway (Homma *et al*, 2019). RAB6-positive (RAB6+) secretory vesicles are transported to the cell surface by two plus end-directed kinesins, KIF5B and KIF13B (Serra-Marques *et al*, 2020). Retrograde transport toward the Golgi apparatus or the endoplasmic reticulum (ER) is driven by dynein (Matanis *et al*, 2002; Young *et al*, 2005). RAB6 recruits dynein and its partner dynactin through Bicaudal-D (BicD) adaptor proteins, leading to dynein activation and processive movement along microtubules (Splinter *et al*, 2012; Mckenney *et al*, 2014; Schlager *et al*, 2014a; Huynh & Vale, 2017; Urnavicius *et al*, 2018). Dynein activity is further regulated by LIS1 (Elshenawy *et al*, 2020; Htet *et al*, 2020; Marzo *et al*, 2020), the dysfunction of which being the most common cause of human lissencephaly (Reiner *et al*, 1993; Marzo *et al*, 2020). LIS1 activates dynein, but can subsequently be released from an idling complex by RAB6 for processing movement (Yamada *et al*, 2013).

In polarized epithelial cells, the machinery controlling trafficking from the Golgi apparatus toward the apical surface was not clearly identified. Conflicting reports have involved both plus-end directed and minus-end directed microtubule motors (Tai *et al*, 1999; Noda *et al*, 2001; Jaulin *et al*, 2007; Bay *et al*, 2013; Aguilar-Aragon *et al*, 2020). This is largely due to the limited ability to resolve vesicular transport and post-Golgi trafficking events in polarized epithelial cells, because of the small size of these cells and to the thickness of epithelial tissues. Here, using a method for subcellular live imaging within embryonic brain slices, we show that apical transport of post-Golgi RAB6+ vesicles is driven by dynein. *RAB6A/B* double KO leads to aRG cell delamination during interphase and to the formation of proliferating RG cells localized basally. *LISbRG1* loss of function largely phenocopies *RAB6A/B* dKO, indicating that the RAB6-dynein-LIS1 apical trafficking pathway is required for preventing aRG cell delamination. Finally, we provide evidence that this pathway is critical for the apical transport of the major polarity determinant CRB3 in aRG cells.

Results

RAB6A/B double knockout causes microcephaly

To investigate the role of RAB6 during mouse neocortex development, we adopted a knockout approach. We confirmed RAB6A/A' and B expression in the developing brain, and observed that RAB6B expression strongly rises from E11.5, while RAB6A/A' levels remain constant (Fig EV1A). Because constitutive knockout of *RAB6A* (coding for the two isoforms RAB6A and RAB6A') leads to early developmental lethality (Shafaq-Zadah *et al*, 2016), we previously generated a Cre-inducible KO mouse model (Bardin *et al*, 2015). Dorsal cortex-specific depletion of *RAB6A*, using the *Emx1-Cre* driver, did not lead to any observable phenotype on neocortex development. To test for redundancy, we therefore generated a constitutive KO mouse for *RAB6B*, using Crispr-Cas9. We obtained two lines, a 279 bp inversion affecting in exons 3 and 4, and a 1 bp deletion in exon 2, both leading to a premature stop codon. Both lines were viable and, as for conditional *RAB6A* KO, did not display any observable alterations of neocortex development. We therefore generated *RAB6A/B* double KO (*RAB6A/B* dKO) animals. Efficient protein depletion for RAB6A/A' and RAB6B in the embryonic cortex was verified by western blot (Fig 1B), residual RAB6A/A' signal in *RAB6A/B* dKO mice being likely due to the presence of non-Cre expressing cells in the protein extract. Strikingly, *RAB6A/B* dKO mice were severely microcephalic. At P0, the cortical area and the cortical thickness of double mutant animals were reduced by half, while single KOs were unaffected (Fig 1C–F). Reduced brain size was likely the consequence of increased levels of apoptotic cell death observed in *RAB6A/B* dKO (Fig 1G). Neuronal positioning was also strongly affected, with layer II-III neurons (CDP+) dispersed throughout the neocortex, suggesting impaired neuronal migration (Fig 1E). Therefore, loss of RAB6A/A' and RAB6B leads to microcephaly and altered neuronal positioning.

RAB6A/B dKO leads to aRG cell delamination during interphase

We next addressed the consequences of *RAB6A/B* dKO on the RG progenitor population. In E15.5 control as well as in single *RAB6A* and *RAB6B* KO brains, these epithelial cells were concentrated within the VZ. In *RAB6*A/B dKO, however, numerous RG cells could be observed above the VZ, suggesting delamination from the neuroepithelium (Fig 2A and B). Moreover, the size of the PAX6+ VZ was reduced, even when normalized to

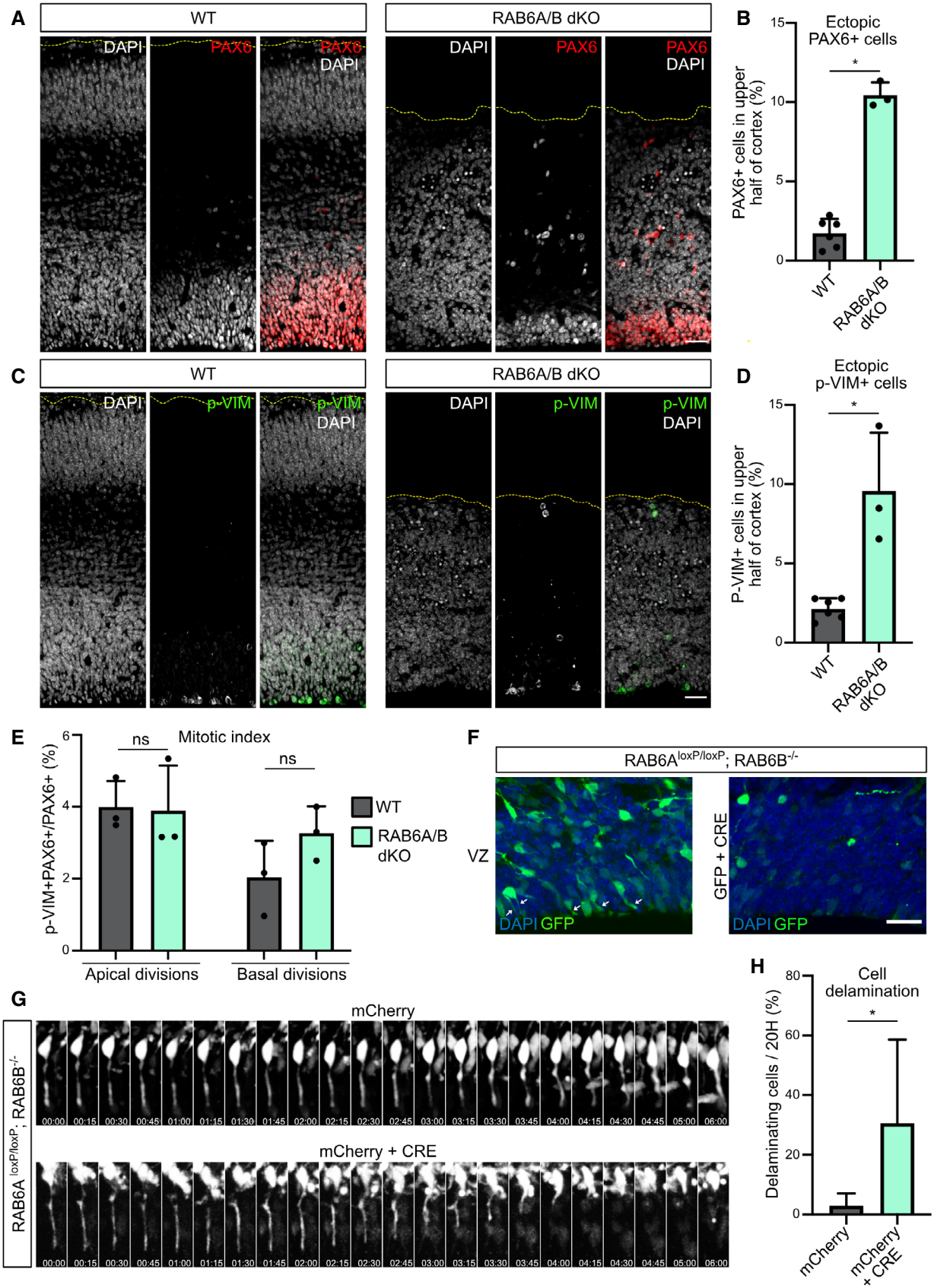

Figure 2.

Figure 2. *RAB6A/B* dKO leads to aRG cell delamination during interphase.

A PAX6 staining in WT and *RAB6A/B* dKO E15.5 brains. Scale bar = 50 μm.
B Percentage of PAX6+ cells located in the upper half of the cortex of WT and *RAB6A/B* dKO E15.5 brains. WT: 4282 cells from $N = 6$ brains. *RAB6A/B* dKO: 1,241 cells from $N = 3$ brains. Mann–Whitney *U* test.
C Phospho-Vimentin (p-Vim) staining in WT and *RAB6A/B* dKO E15.5 brains. Scale bar = 50 μm.
D Percentage p-VIM+ cells dividing ectopically, in the upper half of the cortex of WT and *RAB6A/B dKO* E15.5 brains. WT: 1,713 cells from $N = 6$ brains. *RAB6A/B* dKO: 506 cells from $N = 3$ brains. Mann–Whitney *U* test.
E Mitotic index (p-VIM+ PAX6+ / PAX6+ cells) of RG cells dividing apically (at the ventricular surface) or basally (upper half) in WT and *RAB6A/B* dKO E15.5 brains. Apical divisions: $N = 1{,}886$ cells from 3 brains for WT and 1,511 cells from 3 brains for *RAB6A/B* dKO. Basal divisions: $N = 643$ cells from 3 brains for WT and 809 cells from 3 brains for *RAB6A/B* dKO. Mann–Whitney *U* test.
F Electroporation of $RAB6A^{loxP/loxP}$; $RAB6B^{-/-}$ E14.5 embryos with GFP (control) or GFP + CRE (*RAB6A/B* dKO) and fixation at E18.5. Localization of GFP+ cells in the ventricular zone (VZ). White arrows indicate apical processes. Scale bar = 25 μm.
G Electroporation of $RAB6A^{loxP/loxP}$; $RAB6B^{-/-}$ E14.5 embryos with mCherry (control) or mCherry + CRE (*RAB6A/B* dKO) and live imaging of delamination events at E17.5.
H Apical endfoot detachment and retraction events during 20 h movies in mCherry or mCherry + CRE electroporated cells at E17.5. mCherry: $N = 69$ cells from 5 movies. mCherry + CRE: $N = 52$ cells from 4 movies. Fisher's exact test, $^*P \leq 0.05$.

Data information: All error bars indicate SD.

total cortical thickness, further indicating a loss of ventricular aRG cells (Fig EV1B). The presence of ectopic RG cells was confirmed by the strong increase in the fraction of mitotic RG cells located above the ventricular surface, positive for phospho-Vimentin (p-VIM), which specifically marks mitotic RG cells (Stahl *et al*, 2013; Vaid *et al*, 2018; Fig 2C and D). Both PAX6+ and P-VIM+ ectopic cells were negative for the intermediate progenitor marker TBR2, indicating that differentiation was neither a cause nor a consequence of cell displacement (Fig EV1C–F). P-VIM staining further revealed that basally located RG cells had lost their apical process and had therefore detached form the neuroepithelium. Notably, they had retracted their basal process, and as a consequence could not perform mitotic somal translocation (Ostrem *et al*, 2014) (Fig EV1G). Nevertheless, quantification of the mitotic index of PAX6+ RG cells indicated that ectopic *RAB6A/B* dKO RG cells proliferated at a normal rate (Fig 2E).

To investigate further whether these ectopic aRG cells had indeed delaminated from the neuroepithelium, we used *in utero* electroporation, which specifically targets the aRG cells and therefore allows to assess the position of these cells and their progeny over time (Fig EV1H). We electroporated a plasmid coding for the Cre recombinase, as well as GFP, into E14.5 $RAB6A^{loxP/loxP}$; $RAB6B^{-/-}$ brains, to deplete both RAB6A/A' and B specifically in the GFP-expressing electroporated aRG cells. After 4 days in control GFP-electroporated brains, numerous aRG cells could be observed connected to the ventricular surface by their apical processes (Fig 2F). In Cre-expressing brains however, these cells were largely lost, suggesting that they had detached from the neuroepithelium (Fig 2F). To confirm that the presence of basally localized RG cells was indeed a consequence of apical process detachment during interphase, we live imaged aRG cells 3 days after Cre expression-induced *RAB6A/B* dKO. While the majority of control cells maintained an apical attachment throughout 20 h-long movies, a high proportion of Cre-expressing *RAB6A/B* dKO RG cells were observed to detach from the neuroepithelium and retract their apical process toward the cell soma (Fig 2G and H; Movies EV1 and EV2). Together, these results indicate that double depletion of RAB6A/A' and B leads to the delamination of RG cells during interphase. These cells lose their elongated shape but maintain the expression of RG markers and continue to proliferate above the VZ.

Post-Golgi apical trafficking occurs towards the minus ends of microtubules

To understand how RAB6 may be involved in the maintenance of aRG cell apical attachment to the ventricular surface, we investigated RAB6-dependent post-Golgi transport within the apical process. aRG cells are highly elongated cells and undergo interkinetic nuclear migration (INM), a process by which their nuclei translocate basally, before migrating back to the apical surface for mitosis (Hu *et al*, 2013; Baffet *et al*, 2015). As a consequence, the average distance between the Golgi apparatus, which follows the nucleus, and the apical surface, where the centrosome is located, is 17.84 μm, ranging from 0 to 46.81 μm, depending on the stage of INM (Fig 3A and B; Taverna *et al*, 2016).

To perform subcellular live imaging within thick organotypic brain slices, aRG cells are electroporated with fluorescent reporters *in utero* and, following 24 h of expression, brains are sliced and mounted for imaging on a CSU-W1 spinning disk microscope equipped with a high working distance 100× objective (see methods) (Coquand *et al*, 2021). This approach allowed the visualization of growing microtubule plus ends in cells expressing the plus end tracking protein EB3 (Coquand *et al*, 2021). We confirmed our previous results, that is, the unipolar organization of the microtubule network with over 99% of plus ends growing in the basal direction, from the pericentrosomal apical surface (Fig 3C; Movie EV3). Notably, virtually no microtubules emanating from the Golgi area were observed to grow apically.

To visualize post-Golgi transport vesicles, we electroporated aRG cells *in utero* with a GFP-RAB6A expressing plasmid. The construct was expressed at low levels to avoid cytosolic accumulation, revealing a strong accumulation at the Golgi (Fig 3D). For live imaging, 3–5 planes were imaged to capture the entire apical process, leading to a temporal resolution of 600–1,000 ms. GFP-RAB6A marked the Golgi apparatus, which sometimes appears fragmented as previously reported in these cells (Taverna *et al*, 2016), as well as small and dynamic vesicular structures that could often be observed budding from the Golgi (Fig EV2A; Movie EV4). Live imaging within the apical process (between the Golgi and the apical surface) revealed that RAB6A+ vesicles were bidirectional (Fig 3E; Movie EV5). Highly dynamic RAB6A+ vesicles could also be observed within the basal process (above the nucleus), where they also appeared highly dynamic (Fig EV2B; Movie EV6). In the apical

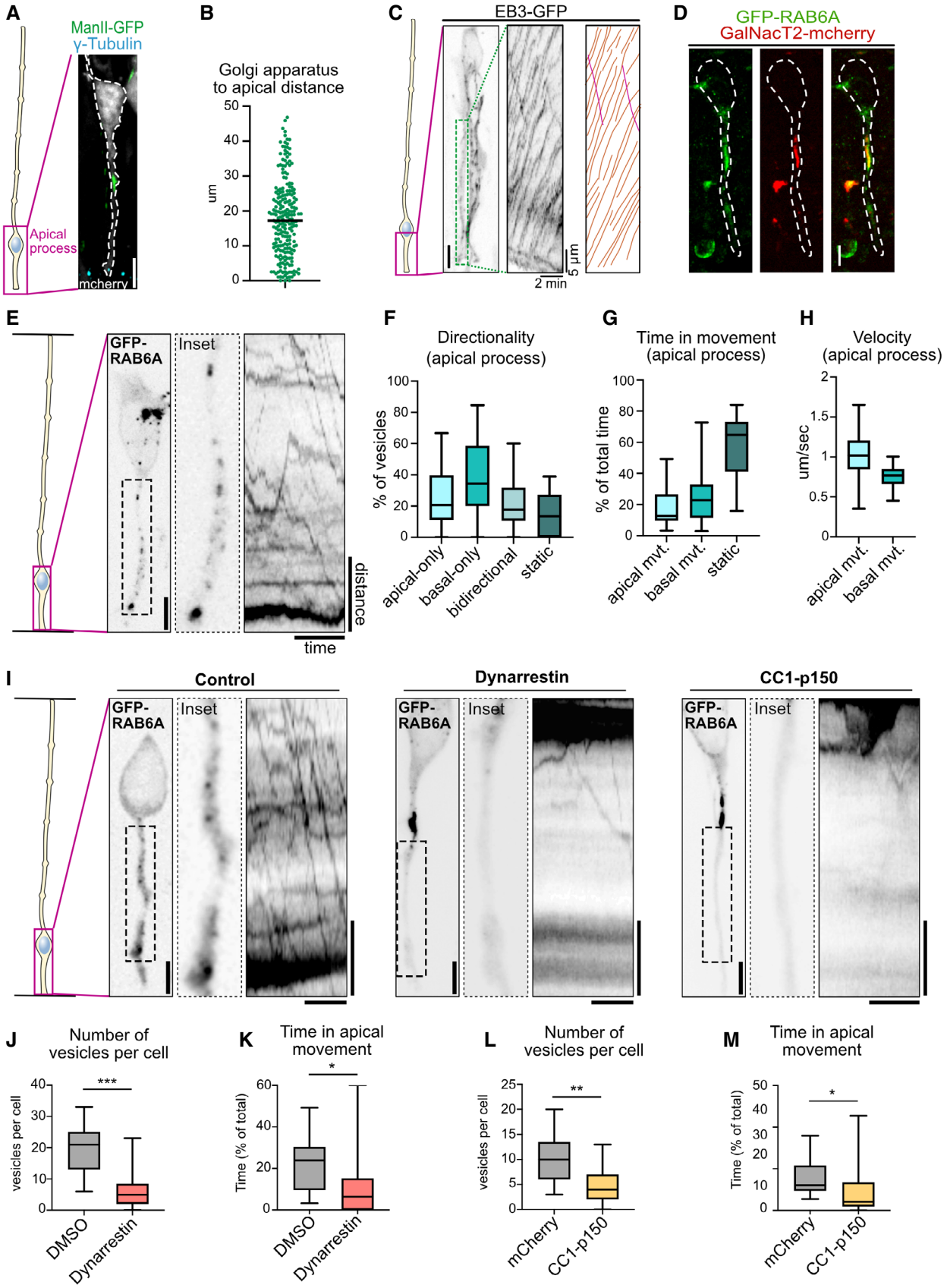

Figure 3.

Figure 3. Apical transport of RAB6A+ post-Golgi vesicles is driven by dynein.

A Localization of the Golgi apparatus (ManII-GFP) and the centrosome (γ-tubulin) in E15.5 mCherry-electroporated radial glial cell. The Golgi apparatus is localized basally, away from the centrosome. Scale bar = 5 μm.
B Average distance between the apical most part of the Golgi apparatus and the apical surface in aRG cells. N = 224 cells from three independent brains.
C Live imaging of EB3-GFP in the apical process of an aRG cell at E15.5. Center: kymograph. Left: manual tracking of EB3 comets. Orange: basally growing. Pink: Apically growing. Scale bar = 5 μm.
D Co-expression of GFP-RAB6A and GalNacT2-mCherry in E15.5 aRG cells reveals colocalization at the Golgi apparatus. Scale bar = 5 μm. Dashed line: cell outline.
E Live imaging of GFP-RAB6A in aRG cells at E15.5 allows tracking of individual RAB6A+ vesicles *in situ*, from the basal Golgi apparatus toward the apical surface. Scale bar = 5 μm. Distance = 5 μm, time = 30 s.
F RAB6A+ vesicle directionality in apical processes of aRG cells over 1-min movies.
G Relative time spent by RAB6A+ vesicles in apical, basal, or static phases.
H Velocity of apically and basally moving RAB6A+ vesicles.
I I Live imaging of GFP-RAB6A in control, dynarrestin-treated, and CC1-p150-expressing aRG cells at E15.5. Scale bars = 5 μm. Distance = 5 μm, time = 30 s.
J Number of RAB6A+ vesicles in the apical process of DMSO and dynarrestin-treated mouse aRG cells.
K Relative time spent by RAB6A+ vesicles in apical movement phase, in DMSO and dynarrestin-treated mouse aRG cells.
L Number of RAB6A+ vesicles in the apical process of mCherry and CC1-p150-expressing aRG cells.
M Relative time spent by RAB6A+ vesicles in apical movement phase, in mCherry and CC1-p150-expressing aRG cells. DMSO treatment slightly affected RAB6A dynamics, as compared to mCherry control.

Data information: (F, G, H) N = 388 vesicles from 30 cells. (J, K, L, M) 216 vesicles from N = 11 cells for DMSO, 145 vesicles from N = 25 cells for dynarrestin, 173 vesicles from N = 17 cells for mCherry control, 71 vesicles from N = 15 cells for CC1-p150. Mann–Whitney U test $^{*}P \leq 0.05$, $^{**}P \leq 0.01$, $^{***}P \leq 0.001$. All boxplots: whiskers indicate min and max, boxes indicate 25th and 75th percentiles, and central band indicates the median.

process, manual tracking of individual RAB6A+ vesicles revealed that, throughout 1-min movies, 39% displayed basal movement (toward the Golgi apparatus), 25% apical movement (toward the apical surface), 21% bidirectional movement, and 15% were static (Fig 3F). These vesicles spent 24% of their time moving in the basal direction, 18% moving in the apical direction, and 58% not moving (Fig 3G). Apically moving RAB6A+ vesicles moved faster than basally moving ones, in agreement with faster minus-end transport reported in non-polarized cells (Schlager *et al*, 2014b; Serra-Marques *et al*, 2020; Fig 3H). Including pauses, RAB6A+ vesicles traveled on average 32.3 μm/min. They were often observed to disappear at the apical surface, suggesting apical fusion events, either with the plasma membrane or with another compartment (Fig EV2C; Movie EV7). Together, these results reveal that RAB6A+ vesicles traffic in a highly bidirectional manner between the perinuclear Golgi apparatus and the apical surface, which they reach following transport directed toward microtubule minus ends.

Apical transport of post-Golgi RAB6A+ vesicles is driven by dynein

We next asked whether post-Golgi apical transport of RAB6A+ vesicles was dependent on the minus end microtubule motor dynein. To test this, we treated brain slices with the dynein inhibitor dynarrestin, prior to live imaging (Höing *et al*, 2018). Because of its short stability, a new batch of dynarrestin was dissolved prior to each experiment, and validated in parallel for Golgi dispersal in RPE-1 cells (Fig EV2D). Dynarrestin treatment in aRG cells led to a drastic inhibition of the trafficking of RAB6A+ vesicles into the apical process, as compared to dimethyl sulfoxide (DMSO)-treated cells (Fig 3I; Movies EV8 and EV9). The total number of RAB6A+ vesicles observed within the apical process was severely reduced (Fig 3J). This result suggests that, in the absence of dynein activity, the balance between opposing motors was shifted toward kinesin-dependent transport in the basal direction, leading to an emptying of the apical process. The vesicles that did manage to enter the apical process performed substantially less apically directed movements (Fig 3K). On the contrary, RAB6A+ vesicles in the cell soma and in the basal process remained highly mobile.

To confirm these results, we next overexpressed a truncated form of p150^{Glued} (CC1-p150), which acts as a dominant negative for the dynactin complex (Tripathy *et al*, 2014). Expression of CC1-p150 for 24 h in aRG cells led to a very similar outcome, impairing the localization of RAB6A+ vesicles into the apical process (Fig 3I and L; Movies EV8 and EV10). As for dynarrestin treatment, apical movement of RAB6A+ vesicles located within the apical process was markedly reduced (Fig 3M). Mobile RAB6A+ vesicles were still abundant in the soma and basal process. In both cells treated with dynarrestin or overexpressing CC1-p150, the speed of RAB6A+ vesicles that were still moving was unaltered within the apical process (Fig EV2E and F). Together, these results indicate that post-Golgi RAB6A+ vesicles travel toward the apical surface of aRG cells along a uniformly polarized microtubule network via dynein-based transport.

Post-Golgi apical transport of Crumbs is driven by dynein

Interphasic delamination is a consequence of destabilization of the adherens junctions, which are themselves dependent on properly established epithelial polarity. The transmembrane protein CRB is a major determinant of epithelial apical domain polarity and the only one to be transported along the secretory pathway. Accordingly, CRB3, the major Crumbs isoform expressed in mammalian epithelial cells (Margolis, 2018), and its partner PALS1 localize to the apical surface of aRG cells (Fig 4A). We therefore asked whether the RAB6-dynein complex controls the apical transport of CRB3 in these cells. To distinguish between different trafficking pools—secretory and endolysosomal—we analyzed CRB3 trafficking using the RUSH system (Boncompain *et al*, 2012; Rodriguez-Fraticelli *et al*, 2015) (Fig 4B). This assay allows for the retention of a cargo of interest in the ER and, upon addition of biotin, its release for trafficking along its secretory route. Following *in utero* electroporation, SBP-CRB3-GFP was efficiently retained *in vivo* within the ER and absent from the apical surface of aRG cells, indicating that endogenous biotin levels in mouse were not sufficient to induce its release (Fig 4C and D). To monitor SBP-CRB3-GFP trafficking, brain slices were incubated in the presence of biotin and fixed at different time points. At

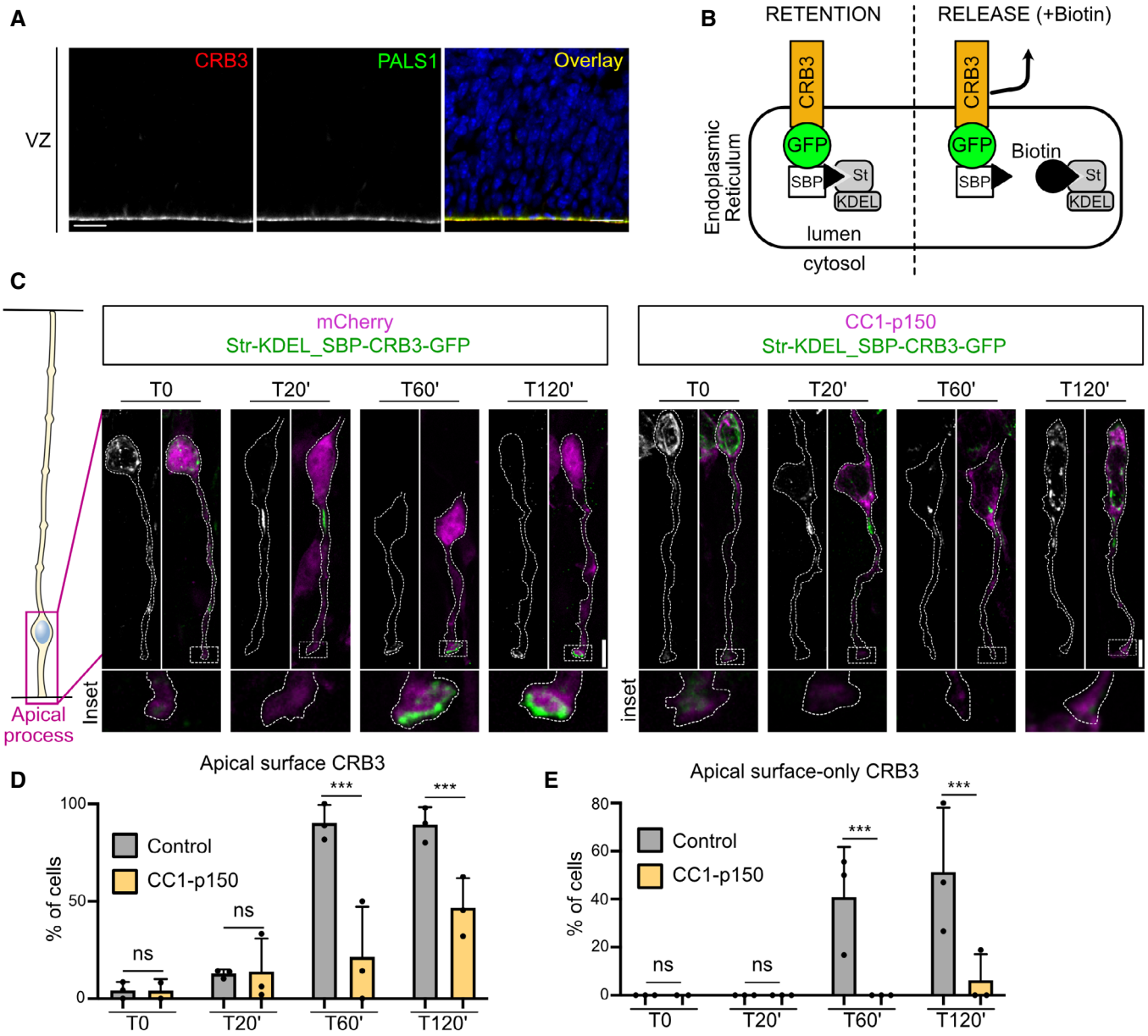

Figure 4. Post-Golgi apical transport of Crumbs is driven by dynein.

A Immuno-staining for Crumbs3 (CRB3) and PALS1 in E15.5 embryonic cortex. Scale bar = 25 μm.

B Schematic representation of the RUSH system. CRB3 is retained in the endoplasmic reticulum (ER) until the addition of biotin, which releases it for trafficking. SBP: Streptavidin-binding protein. St: Streptavidin.

C RUSH assay for CRB3-GFP in control (mcherry) and dynactin-inhibited radial glial cells (CC1-p150-dsRed), electroporated at E.15.5 and imaged at E16.5. Scale bar = 5 μm.

D CRB3 localization at the apical surface upon release.

E Percentage of cells with 100% of CRB3 signal at the apical surface upon release.

Data information: (D, E) mCherry (control): $N = 3$ brains per timepoint (361 cells total). CC1-p150: $N = 3$ brains per timepoint (2 brains for T0) (268 cells total). Fisher's exact test and Benjamini–Hochberg procedure, ***$P \leq 0.001$. All error bars indicate SD.

20 min, CRB3 had arrived at the Golgi apparatus in most aRG cells (95.7 ± 5.2%), and by 60 min it strongly accumulated at the apical surface of over 90% of the cells (Fig 4C and D). In 40% of the cells, CRB3 was only detected at the apical surface, indicating that most of the protein pool had reached its final location (Fig 4C and E). We verified that the bright structure in which CRB3 was released was indeed the Golgi apparatus, by co-expressing the Golgi-resident enzyme GalNacT2. Upon biotin addition, but not before, a strong colocalization between CRB3 and GalNacT2 was indeed observed, confirming Golgi identity (Fig EV3A).

To test whether post-Golgi transport of CRB3 toward the apical surface relies on dynein, we monitored SBP-CRB3-GFP trafficking in

aRG cells expressing the CC1-p150 dominant-negative construct. As in control, 20 min after biotin treatment, CRB3 reached the Golgi apparatus (in 94.1 ± 3.6% of the cells), but at 60 min its trafficking toward the apical surface was severely affected (Fig 4C and D). By 120 min, it started to reach the apical surface, although exhibiting a twofold decrease compared to control cells. Moreover, almost no CC1-expressing cell showed a localization of the total CRB3 pool at the apical surface, even after 120 min, as compared to half of control cells (Fig 4C and E). Therefore, post-Golgi transport of Crumbs towards the apical surface of aRG cells is driven by the dynein–dynactin complex.

We and others have previously shown that post-Golgi RAB6A+ vesicles contain a wide variety of cargoes (Grigoriev *et al*, 2007; Stehbens *et al*, 2014; Fourriere *et al*, 2019). We confirmed here that RAB6A+ vesicles also transport CRB3. HeLa cells expressing CRB3 in the RUSH system were imaged 30 min after biotin addition, when CRB3 has reached the Golgi apparatus and begun to exit it. At this timepoint, almost 80% of vesicles containing SBP-CRB3-GFP were positive for mcherry-RAB6A, indicating that CRB3 largely exits the Golgi apparatus within RAB6A+ vesicles (Fig EV3B and C). To validate that RAB6A+ vesicles also transport CRB3 in aRG cells, we reproduced this experiment within *in vitro* cultivated mouse aRG cells (Fig EV3D and E). Finally, we confirmed these results *in vivo*, within *in utero* electroporated aRG cells (Fig EV3F and G).

LIS1 knockout leads to ectopically dividing progenitors

Because dynein apically transports RAB6+ vesicles containing CRB3, we next asked whether altered dynein would lead to aRG cell delamination, as observed in *RAB6A/B* dKO. To test this, we inactivated the dynein activator *LIS1* in the mouse neocortex, using an inducible KO mouse model (Yingling *et al*, 2008). *Emx1-Cre; LIS1*$^{loxP/loxP}$ (*LIS1* KO) were severely microcephalic, as previously described (Yingling *et al*, 2008). PAX6+ cells in E12.5 *LIS1* KO were found dispersed throughout the entire tissue (Fig 5A). The majority of mitotic RG cells (PAX6+ p-H3+) were localized basally, away from the apical surface where they are normally found, suggesting that they had delaminated (Fig 5A and B). Similarly, we observed a strong increase in the fraction of p-VIM+ cells located above the VZ (Fig 5C and D). As in the *RAB6A/B* dKO, these ectopic pVIM+ cells were largely negative for the intermediate progenitor marker TBR2 (Fig EV4A and B), but had retracted their basal process (Fig EV4C). Therefore, inhibition of dynein through LIS1 loss of function largely phenocopies *RAB6A/B* dKO, suggesting that RAB6-dynein-LIS1-dependent apical trafficking of CRB3 is required to prevent aRG cell delamination.

RAB6A/B and LIS1 are required of CRB localization and maintenance of adherens junctions

To confirm this model, we tested the consequence *of LIS1 and RAB6A/B* KO on the steady-state levels of the Crumbs complex at the apical surface of aRG cells. *LIS1* KO brains revealed altered apical localization of CRB3 and its partner PALS1 (Fig 6A). The CRB3 apical signal intensity was reduced, which we quantified using line scan fluorescent intensity measurements (Fig EV4D). Moreover, we observed the frequent appearance of patches that were completely devoid of CRB3 and PALS1. We quantified the number of empty patches along the ventricular surface, which were completely absent in control embryos but occurred at a frequency of 8.2 per mm in *LIS1* KO embryos (Fig 6B). *RAB6A/B* dKO embryonic cortices also displayed an altered apical localization of CRB3 (Fig 6A). As observed in *LIS1* KO brains, empty patches devoid of CRB3 and PALS1 occurred at a frequency of 4.3 per mm in *RAB6A/B* dKO (Fig 6B). On the other hand, single gene depletion of *RAB6A* or *RAB6B* had no effect.

Finally, to test whether the RAB6/dynein/LIS1 complex is required for proper integrity of the apical junctions, we stained embryonic brains for N-Cadherin. These experiments revealed major junction defects, with abundant interruptions of the staining along the ventricular lining (Fig 6C and D). Even within regions positive for N-Cadherin, the staining was highly abnormal. These results indicate that inhibition of RAB6 and LIS1 alters CRB3 localization and leads to a destabilization of the apical junctions and a delamination of the aRG cells (Fig 6E).

Discussion

A major finding of this study is that, in aRG cells, post-Golgi apical trafficking occurs in the microtubule minus end direction, via the RAB6-dynein-LIS1 complex, and is required for the apical localization of the Crumbs complex (Fig 6E). As a consequence, genetic inactivation of *RAB6A/B* or *LIS1* leads to CRB3 loss at the ventricular surface and a delamination of aRG cells, which maintain RG features, including fate and the ability to proliferate. We also establish aRG cells as a powerful epithelial model, enabling to resolve transport events in real time *in situ*.

Post-Golgi transport is highly bidirectional in aRG cells

Dynein is largely viewed as a retrograde motor, driving trafficking toward the center of the cell. We show here that in epithelial cells, where microtubule minus ends concentrate apically, dynein controls exit from the Golgi apparatus and transport to the apical surface. We observed that apical transport is however highly bidirectional, with RAB6+ vesicles constantly alternating in the apical and basal directions. Therefore, rather than being transported in a strictly polarized manner, RAB6+ vesicles actively oscillate, increasing the chances of reaching and docking to the apical surface. In non-polarized epithelial cells, although bi-directional movement can be observed, the trafficking of post-Golgi RAB6+ vesicles is largely unidirectional, moving toward the cell periphery in a kinesin-dependent manner (Grigoriev *et al*, 2007; Miserey-Lenkei *et al*, 2010; Serra-Marques *et al*, 2020). The higher rate of minus end runs in aRG cells may point to a specific regulation of motors on RAB6+ vesicles upon epithelial polarization. Bicaudal family members, which recruit and activate dynein onto RAB6+ vesicles, are promising candidates for such regulation. Knockout of *BICD2* in the mouse neocortex leads to the appearance of ectopically dividing progenitors, phenocopying *LIS1* and *RAB6A/B* dKO, and suggesting apical polarity defects and delamination (Will *et al*, 2019). Transport in the minus end direction may be further biased by BICDR1, which is able to recruit two dynein molecules for faster movement, and induces strong accumulation of RAB6+ vesicles at the microtubule minus ends (Schlager *et al*, 2010, 2014b; Urnavicius *et al*, 2018).

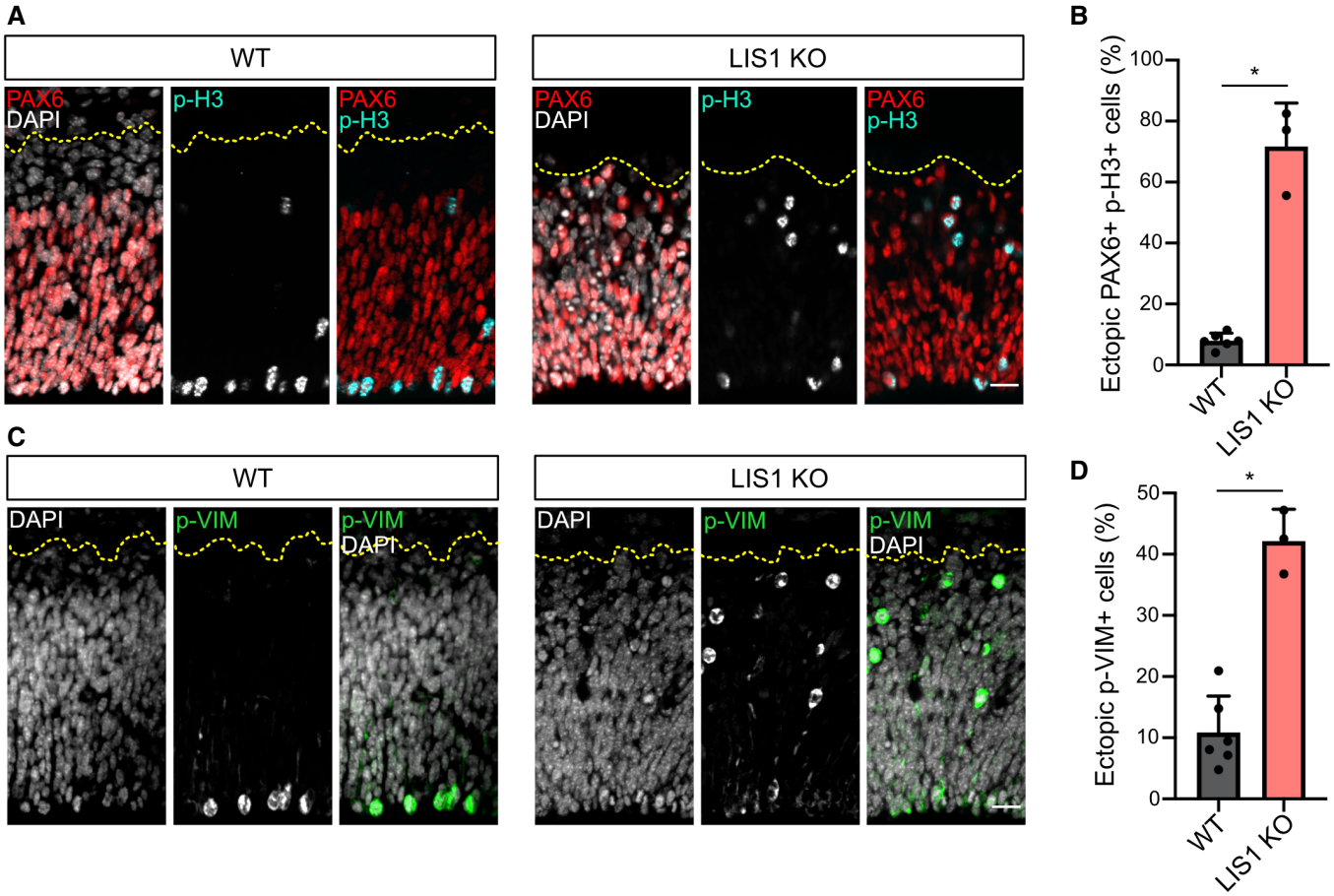

Figure 5. LIS1 knockout leads to ectopically dividing progenitors.

A PAX6 and phospho-Histone 3 (p-H3) staining in WT and *LIS1* KO E12.5 brains. Cortices were subdivided into five bins of equal size along the radial axis. Scale bar = 25 μm.

B Percentage of PH3+/PAX6+ cells located above the ventricular surface of WT and *LIS1* KO E12.5 brains. WT: 1192 cells from $N = 6$ brains. *LIS1* KO: 589 cells from $N = 3$ brains.

C Phospho-Vimentin (p-VIM) staining in WT and *LIS1* KO E12.5 brains. Scale bar = 25 μm.

D Percentage p-VIM+ cells dividing ectopically, away from the ventricular surface of WT and *LIS1* KO E12.5 brains. WT: 1056 cells from $N = 6$ brains. *LIS1* KO: 879 cells from $N = 3$ brains.

Data information: (B, D) Mann–Whitney *U* test, $^*P \leq 0.05$. All error bars indicate SD.

The RAB6-dynein-LIS1 complex controls post-Golgi apical transport of CRB3

Newly synthetized cargoes can traffic directly from the Golgi to the plasma membrane, though passage through intermediate recycling compartments was also proposed. We recently demonstrated that RAB6 acts as a general regulator of protein secretion and confirm here that CRB3 traffics within RAB6+ vesicles (Fourriere *et al*, 2019). Because RAB6+ vesicles directly fuse with the plasma membrane, via its docking factor ELKS (Grigoriev *et al*, 2007), we favor a model whereby CRB3 is directly transported from the Golgi to the apical surface. CRB is known to be further maintained apically through RAB11-dependent and PLLP-dependent recycling route, that leads to its final localization at tight junctions (Rodriguez-Fraticelli *et al*, 2015; Aguilar-Aragon *et al*, 2020). Retromer-dependent transport back to the TGN was also described, indicating that the RAB6-dynein-LIS1 pathway we describe here may also play a role in CRB recycling (Pocha *et al*, 2011). Of note, RAB6+ vesicles were also abundant in the basal process of aRG cells, but the mechanism(s) for sorting of apical and basal post-Golgi cargoes will require further investigation.

RAB6A and RA6B redundantly control polarized trafficking

We observed that, unlike double KO, single deletion of *RAB6A* or *RAB6B* did not affect brain development, indicating that they were largely acting redundantly. Such redundancy was previously observed in cultured neurons following shRNA-mediated knockdown, as well as in MDCK cells where the very low levels of RAB6B are sufficient to compensate for *RAB6A* KO (Schlager *et al*, 2010, 2014b; Homma *et al*, 2019). We also show that RAB6A/A' and RAB6B act redundantly to control proper neuronal positioning,

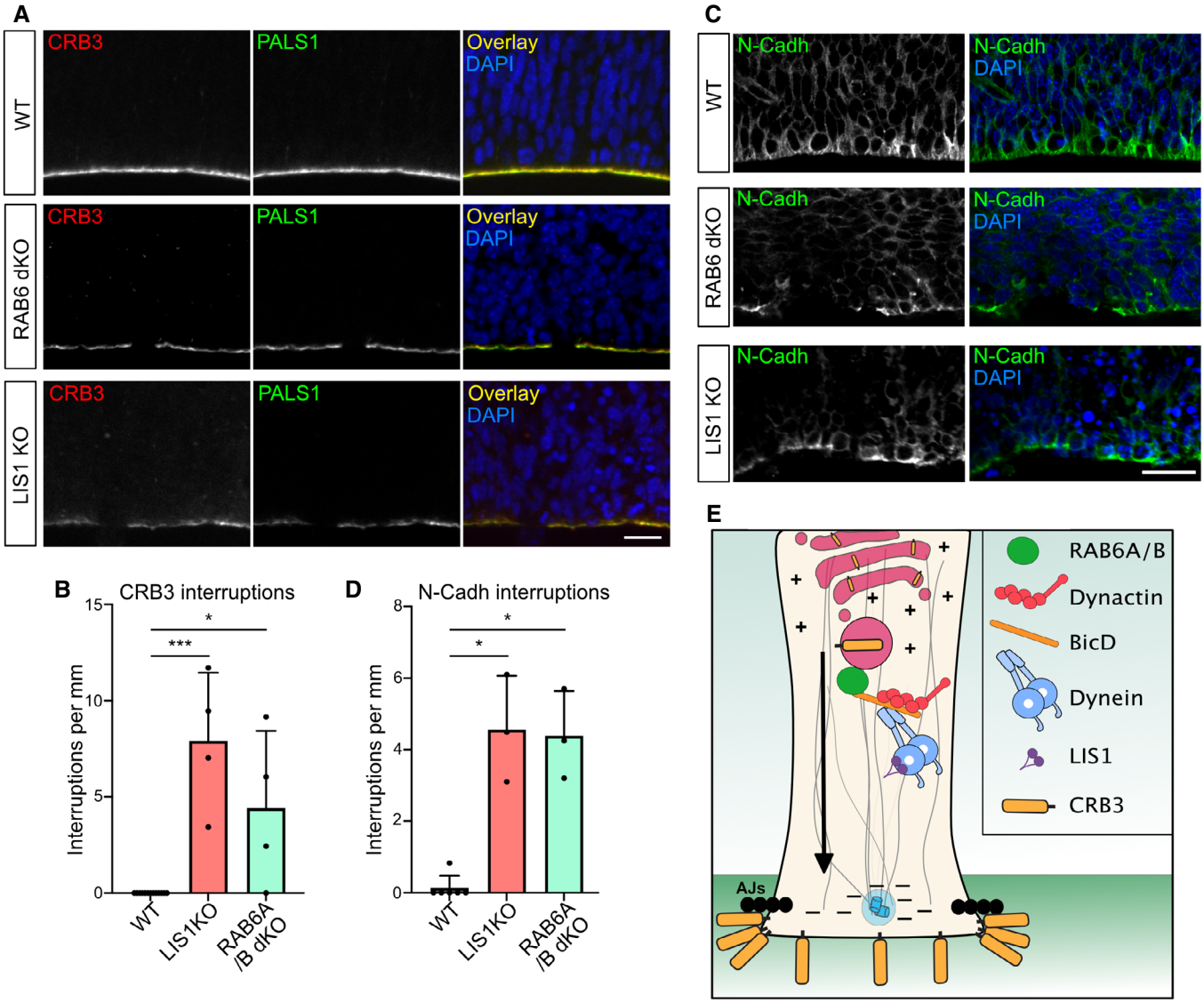

Figure 6. RAB6A/B and LIS1 are required for Crumbs localization and junctional integrity.

A CRB3 and PALS1 staining in WT, *RAB6A/B* dKO (E15.5), and *LIS1* KO (E12.5) brains. Scale bar = 25 μm.

B Quantification of CRB3 staining interruptions along the ventricular boundary of WT (E12.5 and E15.5; N = 13 brains), *LIS1* KO (E12.5, N = 4 brains), and *RAB6A/B* dKO (E15.5, N = 4 brains).

C N-Cadherin staining in WT, *RAB6A/B* dKO (E15.5) and *LIS1* KO (E12.5) brains. Scale bar = 25 μm.

D Quantification of N-Cadh staining interruptions along the ventricular boundary of WT (E12.5 and E15.5; N = 6 brains), *LIS1* KO (E12.5, N = 3 brains), and *RAB6A/B* dKO (E15.5, N = 3 brains).

E Model for post-Golgi apical transport of CRB3 to the apical surface of aRG cells.

Data information: (B, D) Kruskal–Wallis test with a Dunn *post-hoc* test and Benjamini–Hochberg procedure, *$P \leq 0.05$, ***$P \leq 0.001$. All error bars indicate SD.

which may be caused by altered trafficking of adhesion molecules, including integrins (Shafaq-Zadah *et al*, 2016).

Impaired apical post-Golgi trafficking leads to aRG cell delamination

bRG cells are generated from aRG cells and their amplification is a hallmark of gyrencephaly. The expression of several factors is known to affect their production but the underlying mechanisms remain largely unclear (Stahl *et al*, 2013; Florio *et al*, 2015; Ju *et al*, 2016). aRG cells were proposed to detach due to mitotic spindle rotation, or downregulation of the adherens junctions (Konno *et al*, 2008; Ostrem *et al*, 2014; Martínez-Martínez *et al*, 2016). Recent evidence has demonstrated that delamination can be associated with Golgi structure abnormalities, and that detached aRG cells can reintegrate into the epithelium at early developmental stages but not at later neurogenic states (Uzquiano *et al*, 2019; Fujita *et al*, 2020). Here, using live imaging, we

demonstrate that altered post-Golgi transport leads to a detachment of the apical process of aRG cells during interphase, and to the production of ectopically localized cells that maintain RG identity and proliferative capacity. These cells however appear to retract their basal process, potentially due to impaired integrin-based transport to the basal end-foot. We did not observe the appearance of folding patterns in KO brains, due to the presence of an apoptosis-dependent microcephaly phenotype.

In conclusion, our results indicate that the maintenance of epithelial integrity during neocortex development relies on post-Golgi transport to the apical surface of aRG cells. This pathway can control the balance between aRG cell maintenance and delamination, highlighting a site of action for factors that may participate in the generation of bRG cells.

Materials and Methods

Animal breeding and care

Animals

All experiments involving mice were carried out according to the recommendations of the European Community (2010/63/UE). The animals were bred and cared for in the Specific Pathogen Free Animal Facility of Institut Curie (agreement C 75-05-18). All animal procedures were approved by the ethics committee of the Institut Curie CEEA-IC #118 and by French Ministry of Research (2016–002). Animals were housed at a temperature of 22°C, 50% humidity, and a 12/12 h light/dark cycle.

Mice

Generation of RAB6B knockout mice

The constitutive *RAB6B* knockout mice have been engineered using CRISPR/Cas9 technology to create a frame shift in the coding sequence. Two gRNA couples, respectively, targeting exons 2 and 4 (GGAAGACGTCTCTGATCACG and CCGAGACTCCACGGTGGCTG), and 3 and 4 (TGTACTTGGAAGACCGTACG and CAGCTACATCCGAGACTCCA) were selected. gRNAs and Cas9m RNA were prepared according to the online protocol from Feng Zhang, https://www.addgene.org/crispr/zhang/. Briefly, the forward and the reverse oligonucleotides specific for the selected gRNA sequences were annealed and cloned into px330 plasmid. To get Cas9 mRNA and gRNAs, an *in vitro* transcription was performed on Cas9 pCR2.1-XL plasmid and gRNA plasmid using a T7 promoter, and the mMessage mMachine T7 ULTRA kit and MEGAshortscript T7 kit (Life Technologies), respectively. Cas9 mRNA and sgRNAs were then purified using the MEGAclear Kit (Thermo Fisher Scientific) and eluted in RNAse-free water. The gRNAs and Cas9mRNA quality were evaluated on agarose gel.

Eight-week-old superovulated B6D2F1/J (C57BL/6J × DBA/2J) females from Charles River France were superovulated by intraperitoneal (i.p.) administration of 5 IU of Pregnant Mare Serum Gonadotropin followed by an additional i.p. injection of 5 IU Human Chorion Gonadotropin 48 h later. Superovulated females were mated to stud males of the same background. Zygotes were collected from the oviduct and were cultured in Cleave medium (Cook, K-RVCL-50) at 37°C under 5% CO_2 until microinjection. An injection solution was prepared as following: Cas9 mRNA at 100 and 50 ng/µl for each gRNA in Brinster buffer (10 mM Tris–HCl pH 7.5; 0.25 mM EDTA) and passed through 0.22 µm pore size filter. Cytoplasmic microinjection was performed into mouse fertilized oocytes. Microinjected embryos were transferred into 0.5 dpc NMRI pseudopregnant females with 12 zygotes per oviduct. Selected founders F0 carrying a 1 bp deletion in exon 2 and a 279 bp inversion, both leading to a premature STOP codon, were then backcrossed to C57BL6/N to segregate out undesired genetic events.

RAB6A/B dKO and LIS1 KO

RAB6A$^{loxP/loxP}$ mutant mice were previously generated and characterized (Bardin *et al*, 2015). *RAB6A*$^{loxP/loxP}$ mice were first crossed with *RAB6B*$^{-/-}$ mice to generate *RAB6A*$^{loxP/loxP}$; *RAB6B*$^{-/-}$ animals, which were viable and fertile. These animals were then crossed with *Emx1-Cre* (JAX 005628) animals to generate *Emx1*; *RAB6A*$^{loxP/loxP}$; *RAB6B*$^{-/-}$ (*RAB6A/B* double knockout) animals. *LIS1* conditional knockout mice (*LIS1*$^{-/-}$, also known as Pafah1b1-loxP; Hirotsune *et al*, 1998) were crossed with *Emx1-Cre* mice.

Expression constructs and antibodies

The following plasmids were used in this study: ManII-GFP, CC1-p150, Streptavidin-KDEL SBP-CRB3A-GFP (Franck Perez); GFP-RAB6A[54]; EB3-GFP (gift from Matthieu Piel); mCherry2-C1 vector (gift from Michael Davidson, Addgene plasmid #54563); Cre (gift from David Liu, Addgene plasmid #123133); pCAG-Cre-IRES2-GFP vector (gift from Anjen Chenn, Addgene plasmid #26646); pCAG-GFP vector (gift from Richard Vallee, Columbia University); TagRFP-RAB6A (gift from Yuko Mimori-Kiyosue, Riken Center, Japan).

Antibodies used in this study were mouse anti-γTubulin (Sigma-Aldrich, T5326), rat anti-Crumbs3 (gift from André Le Bivic, Marseille), rabbit anti-MPP5/PALS1 (Proteintech, 17710-1-AP), human anti-GFP (recombinant antibody platform (Tab-IP)—Institut Curie, A-R-H#11), rabbit anti-Pax6 (Biolegend, B214847), goat anti-phospho-Histone 3 (Santa Cruz, SC-12927), mouse anti-phospho-Vimentin (Abcam, 22651), CUX-1 (Santa-Cruz, discontinued), rabbit anti-cleaved-Caspase 3 (Cell Signaling, 9661S), rabbit anti-RAB6A/A' (home-made (Goud *et al*, 1990)), rabbit anti-RAB6B (Proteintech, 10340-1-AP), human anti-αTubulin (recombinant antibody platform (Tab-IP)—Institut Curie, A-R-H#02). Secondary antibodies: donkey Alexa Fluor 488 anti-mouse, anti-rabbit, anti-goat (Jackson laboratories 715-545-150, 711-165-152, 715-605-152), donkey Alexa Fluor 555 anti-mouse, anti-rabbit, anti-goat (Jackson laboratories 715-545-150, 711-165-152, 715-605-152), donkey Alexa Fluor 647 anti-mouse, anti-rabbit, anti-goat (Jackson laboratories 715-545-150, 711-165-152, 715-605-152).

Subcellular live imaging in mouse embryonic brain cortex slices

To record GFP-RAB6A dynamics in radial glia *in situ*, we used the following approach. 24 h after the electroporation of E15.5 to E16.5 embryos, the pregnant mouse was sacrificed and the electroporated embryos recovered. Brains were dissected in artificial cerebrospinal fluid (ACSF) and 250-µm thick coronal slices were prepared with a Leica VT1200S vibratome in ice-cold ACSF. The slices were cultured on membrane filters over enriched medium (DMEM-F12 containing B27, N2, 10 ng/ml FGF, 10 ng/ml EGF, 5% fetal bovine serum and

5% horse serum). After recovery in an incubator at 37°C, 5% CO_2 for 2 h (or 48 h for human tissue to allow for construct expression), the filters were cut and carefully turned over on a 35 mm FluoroDish (WPI), to position the sample in direct contact with the glass, underneath the filter (to maintain the sample flat).

Live imaging was performed on a fully motorized spinning disk wide microscope driven by Metamorph software (Molecular Devices) and equipped with a Yokogawa CSU-W1 scanner unit to increase the field of view and improve the resolution deep in the sample. The inverted microscope (Nikon Eclipse Ti2) was equipped with a high working distance (WD 0.3 mm) 100X SR HP Plan Apo 1.35 NA Silicon immersion (Nikon) and a Prime95B sCMOS camera (Photometrics). To maintain stable cell culture conditions (37°C, humidity, 5% CO_2), time-lapse imaging was performed on a STX stage top incubator (Tokai Hit). Z-stacks of 3–5 μm range were taken on a Mad City Lab piezo stage (Nano Z500) with an interval of 1 μm. Maximum projections were generated from which kymographs were generated. Tracking and quantifications of GFP-RAB6A+ vesicle dynamics were directly performed on the movies and the kymographs were used for validation and display purposes. Videos were mounted in Metamorph. Kymograph generation (KymographBuilder), Tracking of GFP-RAB6A+ vesicles (manual tracking) as well as image modifications (brightness and contrast, background, gamma) were carried out on Fiji. Figures were assembled in Affinity Designer.

RUSH assay *in situ*

E15.5–E16.5 embryos were electroporated with a Streptavidin-KDEL SBP-CRB3-GFP construct with or without CC1-p150 for 24 h. Slicing and culture were performed as for subcellular live imaging experiments and sections were cultured in DMEM-F12 medium supplemented with 4 nM avidin to prevent leakage due to circulating biotin. Biotin was added to the enriched medium (40 μM final) for the indicated period of time (37°C, 5% CO2) prior to paraformaldehyde fixation. Immunostaining against GFP was performed to amplify fluorescence (see immunostaining section) prior to mounting.

Statistical analysis

All the statistical analysis has been made using R 4.0.5. R Core Team (2021), R Foundation for Statistical Computing, Vienna, Austria (https://www.R-project.org/). Due to the low sample sizes inherent to *in vivo* work, we conducted nonparametric analyses. Median comparisons between two conditions have been made with a Mann–Whitney *U* test (Figs 2B and D, 3J–M, 5B and D, and EV1B). When more than two conditions were compared, we used Kruskal–Wallis test with a Dunn *post-hoc* test and Benjamini–Hochberg procedure to control the false discovery rate using the dunn.test package (Figs 1D and F, 2E, and 6B and D). These analyses have been made considering the animal as the statistical unit except for the Fig 3J–M. Embryos for a given condition come from different litters. For categorical data (Figs 2H and 4D and E) and data from Figs 3J–M and EV2E and F, we considered each cell as a statistical unit. Since the cells are electroporated *in-situ*, we made the reasonable approximation that cells received their constructs independently and their properties are measured individually at the cell scale. We validated this hypothesis by repeating experiments in different independent animals to conclude that the effect was not due to cells coming from biased individuals due to an abnormal electroporation or an abnormal embryo. For categorial data, analysis has been made using Fisher's exact test (Fig 2H) accompanied with a Benjamini–Hochberg procedure to control the false discovery rate when more than two conditions were compared (Fig 4D and E). These categorical data are depicted as percentages for clarity. *P* values superior to 0.05 are considered as not significant. Due to the evident KO phenotypes, no blinding was performed.

Data availability

No data that require deposition in a public database have been generated.

Expanded View for this article is available online.

Acknowledgements
The authors greatly acknowledge the Cell and Tissue Imaging (PICT-IBiSA), Institut Curie, member of the French National Research Infrastructure France-BioImaging (ANR10-INBS-04), and the Nikon BioImaging Center (Institut Curie, France). We greatly acknowledge the Recombinant Antibody Platform of the Institut Curie for the production of antibodies. We are grateful to Shinji Hirotsune for providing the Lis1 mouse line and embryos, and Yoann Saillour for aid generating Lis1 embryos. We thank D. Massey-Harroche and A. Le Bivic for the anti-Crumbs3 antibody. A.D.B. is an INSERM researcher. This work was supported by the ANR (ANR-19-CE13-0002-02), CNRS, Institut Curie, the Ville de Paris "Emergences" program, Labex CelTisPhyBio (11-LBX-0038), and PSL. F.F.'s lab was supported by the ANR-16-CE16-0011-03 and NEURON-Full-815-006 STEM-MCD grants.

Author contributions
Jean-Baptiste Brault: Conceptualization; data curation; formal analysis; funding acquisition; writing – original draft; project administration. **Sabine Bardin:** Data curation; methodology. **Marusa Lampic:** Data curation. **Jacopo A Carpentieri:** Data curation. **Laure Coquand:** Data curation; methodology. **Maxime Penisson:** Data curation. **Hugo Lachuer:** Formal analysis. **Guiliana Soraya Victoria:** Data curation. **Sarah Baloul:** Data curation. **Fatima El Marjou:** Methodology. **Gaelle Boncompain:** Resources. **Stephanie Miserey-Lenkei:** Resources. **Richard Belvindrah:** Data curation. **Vincent Fraisier:** Methodology. **Fiona Francis:** Resources. **Franck Perez:** Resources; funding acquisition; methodology. **Bruno Goud:** Conceptualization; formal analysis; writing – original draft; project administration; writing – review and editing. **Alexandre D Baffet:** Conceptualization; data curation; formal analysis; funding acquisition; investigation; visualization; methodology; writing – original draft; project administration; writing – review and editing.

Disclosure and competing interests statement
The authors declare that they have no conflict of interest.

References

Aguilar-Aragon M, Fletcher G, Thompson BJ (2020) The cytoskeletal motor proteins dynein and MyoV direct apical transport of Crumbs. *Dev Biol* 459: 126 – 137

Apodaca G, Gallo LI, Bryant DM (2012) Role of membrane traffic in the generation of epithelial cell asymmetry. *Nat Cell Biol* 14: 1235 – 1243

Baffet AD, Hu DJ, Vallee RB (2015) Cdk1 activates pre-mitotic nuclear envelope dynein recruitment and apical nuclear migration in neural stem cells. *Dev Cell* 33: 703 – 716

Bardin S, Miserey-Lenkei S, Hurbain I, Garcia-Castillo D, Raposo G, Goud B (2015) Phenotypic characterisation of RAB6A knockout mouse embryonic fibroblasts. *Biol Cell* 107: 427 – 439

Bay AEP, Schreiner R, Mazzoni F, Carvajal-Gonzalez JM, Gravotta D, Perret E, Mantaras GL, Zhu Y-S, Rodriguez-Boulan EJ (2013) The kinesin KIF16B mediates apical transcytosis of transferrin receptor in AP-1B-deficient epithelia. *EMBO J* 32: 2125 – 2139

Boncompain G, Divoux S, Gareil N, de Forges H, Lescure A, Latreche L, Mercanti V, Jollivet F, Raposo G, Perez F (2012) Synchronization of secretory protein traffic in populations of cells. *Nat Methods* 9: 493 – 498

Bulgakova NA, Knust E (2009) The Crumbs complex: From epithelial-cell polarity to retinal degeneration. *J Cell Sci* 122: 2587 – 2596

Cappello S, Attardo A, Wu X, Iwasato T, Itohara S, Wilsch-Bräuninger M, Eilken HM, Rieger MA, Schroeder TT, Huttner WB *et al* (2006) The rho-GTPase cdc42 regulates neural progenitor fate at the apical surface. *Nat Neurosci* 9: 1099 – 1107

Coquand L, Victoria GS, Tata A, Carpentieri JA, Brault J-B, Guimiot F, Fraisier V, Baffet AD (2021) CAMSAPs organize an acentrosomal microtubule network from basal varicosities in radial glial cells. *J Cell Biol* 220: e202003151

Dudok JJ, Murtaza M, Alves CH, Rashbass P, Wijnholds J (2016) Crumbs 2 prevents cortical abnormalities in mouse dorsal telencephalon. *Neurosci Res* 108: 12 – 23

Elshenawy MM, Kusakci E, Volz S, Baumbach J, Bullock SL, Yildiz A (2020) Lis1 activates dynein motility by modulating its pairing with dynactin. *Nat Cell Biol* 22: 570 – 578

Fernández V, Llinares-Benadero C, Borrell V (2016) Cerebral cortex expansion and folding: what have we learned? *EMBO J* 35: 1021 – 1044

Fietz SA, Kelava I, Vogt J, Wilsch-Bräuninger M, Stenzel D, Fish JL, Corbeil D, Riehn A, Distler W, Nitsch R *et al* (2010) OSVZ progenitors of human and ferret neocortex are epithelial-like and expand by integrin signaling. *Nat Neurosci* 13: 690 – 699

Florio M, Albert M, Taverna E, Namba T, Brandl H, Lewitus E, Haffner C, Sykes A, Wong FK, Peters J *et al* (2015) Human-specific gene ARHGAP11B promotes basal progenitor amplification and neocortex expansion. *Science* 347: 1465 – 1470

Florio M, Borrell V, Huttner WB (2016) Human-specific genomic signatures of neocortical expansion. *Curr Opin Neurobiol* 42: 33 – 44

Fourriere L, Kasri A, Gareil N, Bardin S, Bousquet H, Pereira D, Perez F, Goud B, Boncompain G, Miserey-Lenkei S (2019) RAB6 and microtubules restrict protein secretion to focal adhesions. *J Cell Biol* 218: 2215 – 2231

Fujita I, Shitamukai A, Kusumoto F, Mase S, Suetsugu T, Omori A, Kato K, Abe T, Shioi G, Konno D *et al* (2020) Endfoot regeneration restricts radial glial state and prevents translocation into the outer subventricular zone in early mammalian brain development. *Nat Cell Biol* 22: 26 – 37

Goud B, Zahraoui A, Tavitian A, Saraste J (1990) Small GTP-binding protein associated with Golgi cisternae. *Nature* 345: 553 – 556

Goud B, Liu S, Storrie B (2018) Rab proteins as major determinants of the Golgi complex structure. *Small GTPases* 9: 66 – 75

Grigoriev I, Splinter D, Keijzer N, Wulf PS, Demmers J, Ohtsuka T, Modesti M, Maly IV, Grosveld F, Hoogenraad CC *et al* (2007) Rab6 regulates transport and targeting of exocytotic carriers. *Dev Cell* 13: 305 – 314

Hansen DV, Lui JH, Parker PRL, Kriegstein AR (2010) Neurogenic radial glia in the outer subventricular zone of human neocortex. *Nature* 464: 554 – 561

Hirotsune S, Fleck MW, Gambello MJ, Bix GJ, Chen A, Clark GD, Ledbetter DH, McBain CJ, Wynshaw-Boris A (1998) Graded reduction of Pafah1b1 (Lis1) activity results in neuronal migration defects and early embryonic lethality. *Nat Genet* 19: 333 – 339

Höing S, Yeh T-Y, Baumann M, Martinez NE, Habenberger P, Kremer L, Drexler HCA, Küchler P, Reinhardt P, Choidas A *et al* (2018) Dynarrestin, a novel inhibitor of cytoplasmic dynein. *Cell Chem Biol* 25: 357 – 369.e6

Homma Y, Kinoshita R, Kuchitsu Y, Wawro PS, Marubashi S, Oguchi ME, Ishida M, Fujita N, Fukuda M (2019) Comprehensive knockout analysis of the Rab family GTPases in epithelial cells. *J Cell Biol* 218: 2035 – 2050

Htet ZM, Gillies JP, Baker RW, Leschziner AE, DeSantis ME, Reck-Peterson SL (2020) LIS1 promotes the formation of activated cytoplasmic dynein-1 complexes. *Nat Cell Biol* 22: 518 – 525

Hu DJ-K, Baffet AD, Nayak T, Akhmanova AS, Doye V, Vallee RB (2013) Dynein recruitment to nuclear pores activates apical nuclear migration and mitotic entry in brain progenitor cells. *Cell* 154: 1300 – 1313

Huynh W, Vale RD (2017) Disease-associated mutations in human BICD2 hyperactivate motility of dynein-dynactin. *J Cell Biol* 216: 3051 – 3060

Itoh Y, Moriyama Y, Hasegawa T, Endo TA, Toyoda T, Gotoh Y (2013) Scratch regulates neuronal migration onset via an epithelial-mesenchymal transition–like mechanism. *Nat Neurosci* 16: 1 – 12

Jaulin F, Xue X, Rodriguez-Boulan E, Kreitzer G (2007) Polarization-dependent selective transport to the apical membrane by KIF5B in MDCK cells. *Dev Cell* 13: 511 – 522

Johnson MB, Sun X, Kodani A, Borges-Monroy R, Girskis KM, Ryu SC, Wang PP, Patel K, Gonzalez DM, Woo YM *et al* (2018) Aspm knockout ferret reveals an evolutionary mechanism governing cerebral cortical size. *Nature* 556: 370 – 375

Ju X-C, Hou Q-Q, Sheng A-L, Wu K-Y, Zhou Y, Jin Y, Wen T, Yang Z, Wang X, Luo Z-G (2016) The hominoid-specific gene TBC1D3 promotes generation of basal neural progenitors and induces cortical folding in mice. *eLife* 5: e18197

Kim S, Lehtinen MK, Sessa A, Zappaterra MW, Cho S-H, Gonzalez D, Boggan B, Austin CA, Wijnholds J, Gambello MJ *et al* (2010) The apical complex couples cell fate and cell survival to cerebral cortical development. *Neuron* 66: 69 – 84

Konno D, Shioi G, Shitamukai A, Mori A, Kiyonari H, Miyata T, Matsuzaki F (2008) Neuroepithelial progenitors undergo LGN-dependent planar divisions to maintain self-renewability during mammalian neurogenesis. *Nat Cell Biol* 10: 93 – 101

Lee HO, Norden C (2013) Mechanisms controlling arrangements and movements of nuclei in pseudostratified epithelia. *Trends Cell Biol* 23: 141 – 150

Margolis B (2018) The Crumbs3 polarity protein. *Cold Spring Harb Perspect Biol* 10: a027961

Martínez-Martínez MÁ, Romero CDJ, Fernández V, Cárdenas A, Götz M, Borrell V (2016) A restricted period for formation of outer subventricular zone defined by Cdh1 and Trnp1 levels. *Nat Commun* 7: 11812

Marzo MG, Griswold JM, Markus SM (2020) Pac1/LIS1 stabilizes an uninhibited conformation of dynein to coordinate its localization and activity. *Nat Cell Biol* 22: 559 – 569

Matanis T, Akhmanova AS, Wulf P, Nery ED, Weide T, Stepanova T, Galjart N, Grosveld F, Goud B, de Zeeuw CI *et al* (2002) Bicaudal-D regulates COPI-independent Golgi–ER transport by recruiting the dynein–dynactin motor complex. *Nat Cell Biol* 4: 986 – 992

Mckenney RJ, Huynh W, Tanenbaum ME, Bhabha G, Vale RD (2014) Activation of cytoplasmic dynein motility by dynactin-cargo adapter complexes. *Science* 345: 337 – 341

Miserey-Lenkei S, Chalancon G, Bardin S, Formstecher E, Goud B, Echard A (2010) Rab and actomyosin-dependent fission of transport vesicles at the Golgi complex. *Nat Cell Biol* 12: 645 – 654

Narayanan R, Pham L, Kerimoglu C, Watanabe T, Hernandez RC, Sokpor G, Ulmke PA, Kiszka KA, Tonchev AB, Rosenbusch J *et al* (2018) Chromatin remodeling BAF155 subunit regulates the genesis of basal progenitors in developing cortex. *iScience* 4: 109 – 126

Noda Y, Okada Y, Saito N, Setou M, Xu Y, Zhang Z, Hirokawa N (2001) KIFC3, a microtubule minus end-directed motor for the apical transport of annexin XIIIb-associated triton-insoluble membranes. *J Cell Biol* 155: 77 – 88

Opdam FJ, Echard A, Croes HJ, van den Hurk JA, van de Vorstenbosch RA, Ginsel LA, Goud B, Fransen JA (2000) The small GTPase Rab6B, a novel Rab6 subfamily member, is cell-type specifically expressed and localised to the Golgi apparatus. *J Cell Sci* 113: 2725 – 2735

Ostrem BEL, Lui JH, Gertz CC, Kriegstein AR (2014) Control of outer radial glial stem cell mitosis in the human brain. *Cell Rep* 8: 656 – 664

Paridaen JT, Huttner WB (2014) Neurogenesis during development of the vertebrate central nervous system. *EMBO Rep* 15: 351 – 364

Penisson M, Ladewig J, Belvindrah R, Francis F (2019) Genes and mechanisms involved in the generation and amplification of basal radial glial cells. *Front Cell Neurosci* 13: 381

Pocha SM, Wassmer T, Niehage C, Hoflack B, Knust E (2011) Retromer controls epithelial cell polarity by trafficking the apical determinant Crumbs. *Curr Biol* 21: 1111 – 1117

Reillo I, Romero CDJ, García-Cabezas MÁ, Borrell V (2011) A role for intermediate radial glia in the tangential expansion of the mammalian cerebral cortex. *Cereb Cortex* 21: 1674 – 1694

Reiner O, Carrozzo R, Shen Y, Wehnert M, Faustinella F, Dobyns WB, Caskey CT, Ledbetter DH (1993) Isolation of a miller-Dieker lissencephaly gene containing G protein beta-subunit-like repeats. *Nature* 364: 717 – 721

Rodriguez-Boulan E, Macara IG (2014) Organization and execution of the epithelial polarity programme. *Nat Rev Mol Cell Biol* 15: 225 – 242

Rodriguez-Fraticelli AE, Bagwell J, Bosch-Fortea M, Boncompain G, Reglero-Real N, García-León MJ, Andrés G, Toribio ML, Alonso MA, Millán J *et al* (2015) Developmental regulation of apical endocytosis controls epithelial patterning in vertebrate tubular organs. *Nat Cell Biol* 17: 241 – 250

Schlager MA, Kapitein LC, Grigoriev I, Burzynski GM, Wulf PS, Keijzer N, de Graaff E, Fukuda M, Shepherd IT, Akhmanova AS *et al* (2010) Pericentrosomal targeting of Rab6 secretory vesicles by bicaudal-D-related protein 1 (BICDR-1) regulates neuritogenesis. *EMBO J* 29: 1637 – 1651

Schlager MA, Hoang HT, Urnavicius L, Bullock SL, Carter AP (2014a) *In vitro* reconstitution of a highly processive recombinant human dynein complex. *EMBO J* 33: 1855 – 1868

Schlager MA, Serra-Marques A, Grigoriev I, Gumy LF, da Silva ME, Wulf PS, Akhmanova AS, Hoogenraad CC (2014b) Bicaudal D family adaptor proteins control the velocity of dynein-based movements. *Cell Rep* 8: 1248 – 1256

Serra-Marques A, Martin M, Katrukha EA, Grigoriev I, Peeters CA, Liu Q, Hooikaas PJ, Yao Y, Solianova V, Smal I *et al* (2020) Concerted action of kinesins KIF5B and KIF13B promotes efficient secretory vesicle transport to microtubule plus ends. *eLife* 9: e61302

Shafaq-Zadah M, Gomes-Santos CS, Bardin S, Maiuri P, Maurin M, Iranzo J, Gautreau A, Lamaze C, Caswell P, Goud B *et al* (2016) Persistent cell migration and adhesion rely on retrograde transport of β(1) integrin. *Nat Cell Biol* 18: 54 – 64

Splinter D, Razafsky DS, Schlager MA, Serra-Marques A, Grigoriev I, Demmers J, Keijzer N, Jiang K, Poser I, Hyman AA *et al* (2012) BICD2, dynactin, and LIS1 cooperate in regulating dynein recruitment to cellular structures. *Mol Biol Cell* 23: 4226 – 4241

Stahl R, Walcher T, Romero CDJ, Pilz GA, Cappello S, Irmler M, Sanz-Aquela JM, Beckers J, Blum R, Borrell V *et al* (2013) Trnp1 regulates expansion and folding of the mammalian cerebral cortex by control of radial glial fate. *Cell* 153: 535 – 549

Stehbens SJ, Paszek M, Pemble H, Ettinger A, Gierke S, Wittmann T (2014) CLASPs link focal-adhesion-associated microtubule capture to localized exocytosis and adhesion site turnover. *Nat Cell Biol* 16: 561 – 573

Tai AW, Chuang JZ, Bode C, Wolfrum U, Sung CH (1999) Rhodopsin's carboxy-terminal cytoplasmic tail acts as a membrane receptor for cytoplasmic dynein by binding to the dynein light chain Tctex-1. *Cell* 97: 877 – 887

Tavano S, Taverna E, Kalebic N, Haffner C, Namba T, Dahl A, Wilsch-Bräuninger M, Paridaen JTML, Huttner WB (2018) Insm1 induces neural progenitor delamination in developing neocortex via downregulation of the Adherens Junction Belt-specific protein Plekha7. *Neuron* 97: 1299 – 1314.e8

Taverna E, Mora-Bermúdez F, Strzyz PJ, Florio M, Icha J, Haffner C, Norden C, Wilsch-Bräuninger M, Huttner WB (2016) Non-canonical features of the Golgi apparatus in bipolar epithelial neural stem cells. *Sci Rep* 6: 21206

Tripathy SK, Weil SJ, Chen C, Anand P, Vallee RB, Gross SP (2014) Autoregulatory mechanism for dynactin control of processive and diffusive dynein transport. *Nat Cell Biol* 16: 1192 – 1201

Urnavicius L, Lau CK, Elshenawy MM, Morales-Rios E, Motz C, Yildiz A, Carter AP (2018) Cryo-EM shows how dynactin recruits two dyneins for faster movement. *Nature* 554: 202 – 206

Uzquiano A, Ng IG, Nguyen L, Reiner O, Götz M, Matsuzaki F, Francis F (2018) Cortical progenitor biology: Key features mediating proliferation versus differentiation. *J Neurochem* 146: 500 – 525

Uzquiano A, Cifuentes-Diaz C, Jabali A, Romero DM, Houllier A, Dingli F, Maillard C, Boland A, Deleuze J-F, Loew D *et al* (2019) Mutations in the heterotopia gene Eml1/EML1 severely disrupt the formation of primary cilia. *Cell Rep* 28: 1596 – 1611.e10

Vaid S, Camp JG, Hersemann L, Oegema CE, Heninger A-K, Winkler S, Brandl H, Sarov M, Treutlein B, Huttner WB *et al* (2018) A novel population of Hopx-dependent basal radial glial cells in the developing mouse neocortex. *Development* 145: dev169276

Will L, Portegies S, van Schelt J, van Luyk M, Jaarsma D, Hoogenraad CC (2019) Dynein activating adaptor BICD2 controls radial migration of upper-layer cortical neurons *in vivo*. *Acta Neuropathol Commun* 7: 162 – 123

Yamada M, Kumamoto K, Mikuni S, Arai Y, Kinjo M, Nagai T, Tsukasaki Y, Watanabe TM, Fukui M, Jin M *et al* (2013) Rab6a releases LIS1 from a dynein idling complex and activates dynein for retrograde movement. *Nat Commun* 4: 2033

Yingling J, Youn YH, Darling D, Toyo-oka K, Pramparo T, Hirotsune S, Wynshaw-Boris A (2008) Neuroepithelial stem cell proliferation requires LIS1 for precise spindle orientation and symmetric division. *Cell* 132: 474 – 486

Young J, Stauber T, Nery ED, Vernos I, Pepperkok R, Nilsson T (2005) Regulation of microtubule-dependent recycling at the trans-Golgi network by Rab6A and Rab6A'. *Mol Biol Cell* 16: 162 – 177

Expanded View Figures

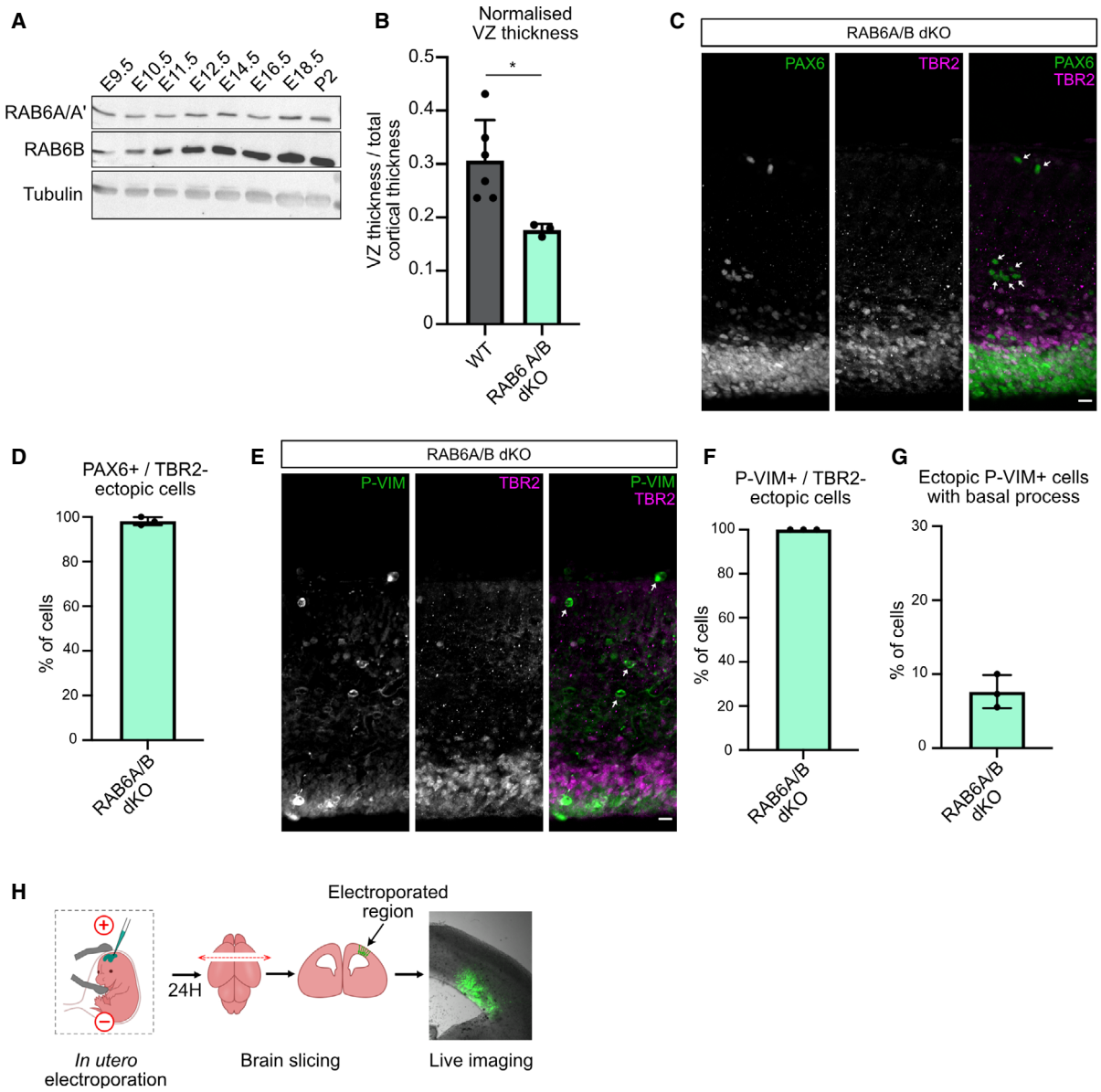

Figure EV1. RAB6 A/B dKO leads to ectopic TBR2-negative basal progenitors.

A RAB6A/A' and RAB6B expression in the developing brain and at P2.
B Ventricular zone (VZ) thickness normalized to total cortical thickness in $N = 6$ WT brains and $N = 3$ *RAB6A/B* dKO. Mann–Whitney *U* test, $*P \leq 0.05$.
C PAX6 and TBR2 staining in *RAB6A/B* dKO E15.5 brains. Arrows indicate detached PAX6+/TBR2− cells. Scale bar = 25 μm.
D Percentage of ectopic PAX6+/TBR2− cells in *RAB6A/B* dKO E15.5 brains. *RAB6A/B* dKO: 470 cells from $N = 3$ brains.
E P-VIM and TBR2 staining in *RAB6A/B* dKO E15.5 brains. Arrows indicate detached P-VIM+/TBR2− cells. Scale bar = 25 μm.
F Percentage of ectopic P-VIM+/TBR2− cells in *RAB6A/B* dKO E15.5 brains. *RAB6A/B* dKO: 99 cells from $N = 3$ brains.
G Percentage of ectopic P-VIM+ cells that maintained a basal process in *RAB6A/B* dKO E15.5 brains. *RAB6A/B* dKO: 99 cells from $N = 3$ brains.
H Schematic representation of *in utero* electroporation and live imaging procedure in the mouse developing cortex.

Data information: All error bars indicate SD.

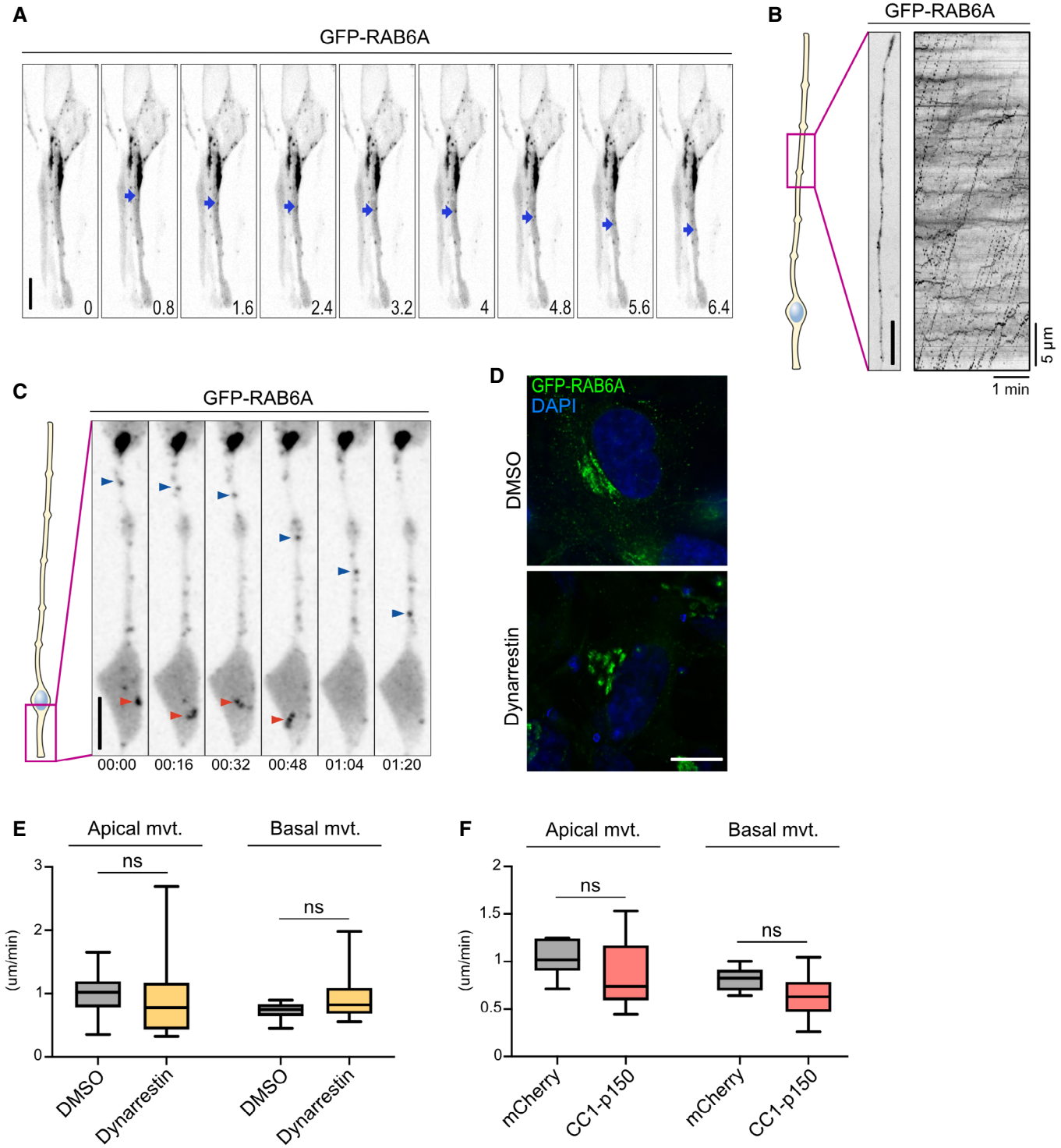
A
GFP-RAB6A
0
0.8
1.6
2.4
3.2
4
4.8
5.6
6.4
B
GFP-RAB6A
5 µm
1 min
C
GFP-RAB6A
00:00
00:16
00:32
00:48
01:04
01:20
D
GFP-RAB6A
DAPI
DMSO
Dynarrestin
E
Apical mvt.
Basal mvt.
ns
ns
(um/min)
DMSO
Dynarrestin
DMSO
Dynarrestin
F
Apical mvt.
Basal mvt.
ns
ns
(um/min)
mCherry
CC1-p150
mCherry
CC1-p150

Figure EV2.

Figure EV2. RAB6A dynamics in aRG cells and dynarrestin validation.

A Live imaging of GFP-RAB6A in the apical process of an aRG cell at E15.5. At 0.8 s, a tubule is budding from the Golgi, leading to the formation of an apically moving vesicle. Blue arrowhead indicates RAB6A+ vesicle. Scale bar = 5 μm.
B Live imaging of GFP-RAB6A in the basal process of an aRG cell at E15.5. Right: kymograph. Scale bar = 5 μm.
C Live imaging of GFP-RAB6A in the apical process of an aRG cell at E15.5. Red arrowhead: a RAB6A+ vesicle can be seen disappearing in the endfoot, suggesting fusion with the apical membrane. Blue arrowhead: a RAB6A+ vesicle moving apically within the apical process. Scale bar = 10 μm.
D RPE-1 cells transfected with GFP-RAB6A to visualize the Golgi apparatus architecture, and treated for 4 h with 100 μM dynarrestin or DMSO. Scale bar = 10 μm.
E Velocity of apically and basally moving RAB6A vesicles within the apical process of DMSO and dynarrestin-treated aRG cells. In all, 142 vesicles from $N = 7$ cells for DMSO, 74 vesicles from $N = 18$ cells for dynarrestin.
F Velocity of apically and basally moving RAB6A vesicles within the apical process of mcherry control and CC1-p150-expressing aRG cells. In all, 120 vesicles from $N = 17$ cells for mCherry control, 39 vesicles from $N = 11$ cells for CC1-p150.

Data information: (E, F) Mann–Whitney *U* test. Boxplots whiskers indicate min and max, boxes indicate 25th and 75th percentiles, and central band indicates the median.

Figure EV3. CRB3 exits the Golgi within RAB6+ vesicles.

A SBP-CRB3-GFP and GalNacT2-mCherry expression in aRG cells before and 45 min after addition of biotin. SBP-CRB3-GFP relocates from a diffuse perinuclear localization to the Golgi. Scale bar = 5 μm.
B SBP-CRB3-GFP and mCherry-RAB6A localization in HeLa cells before and 40 min after addition of biotin. Scale bar = 5 μm. White arrowheads: colocalizing foci.
C Quantification of SBP-CRB3-GFP and mCherry-RAB6A colocalization away from the Golgi apparatus 40 min after biotin addition. $N = 16$ cells from three independent experiments.
D SBP-CRB3-GFP and mCherry-RAB6A localization in dissociated aRG cells cultivated *in vitro*, 40 min after addition of biotin. Scale bar = 5 μm. Yellow arrowheads: colocalizing foci.
E Quantification of SBP-CRB3-GFP and mCherry-RAB6A colocalization away from the Golgi apparatus 40 min after biotin addition. $N = 14$ cells from three independent experiments.
F SBP-CRB3-GFP and mCherry-RAB6A localization in aRG cells cultivated within brain slices, 40 min after addition of biotin. Scale bar = 5 μm. Yellow arrowheads: colocalizing foci.
G Quantification of SBP-CRB3-GFP and mCherry-RAB6A colocalization away from the Golgi apparatus 40 min after biotin addition. $N = 15$ cells from three independent experiments.

Data information: All error bars indicate SD.

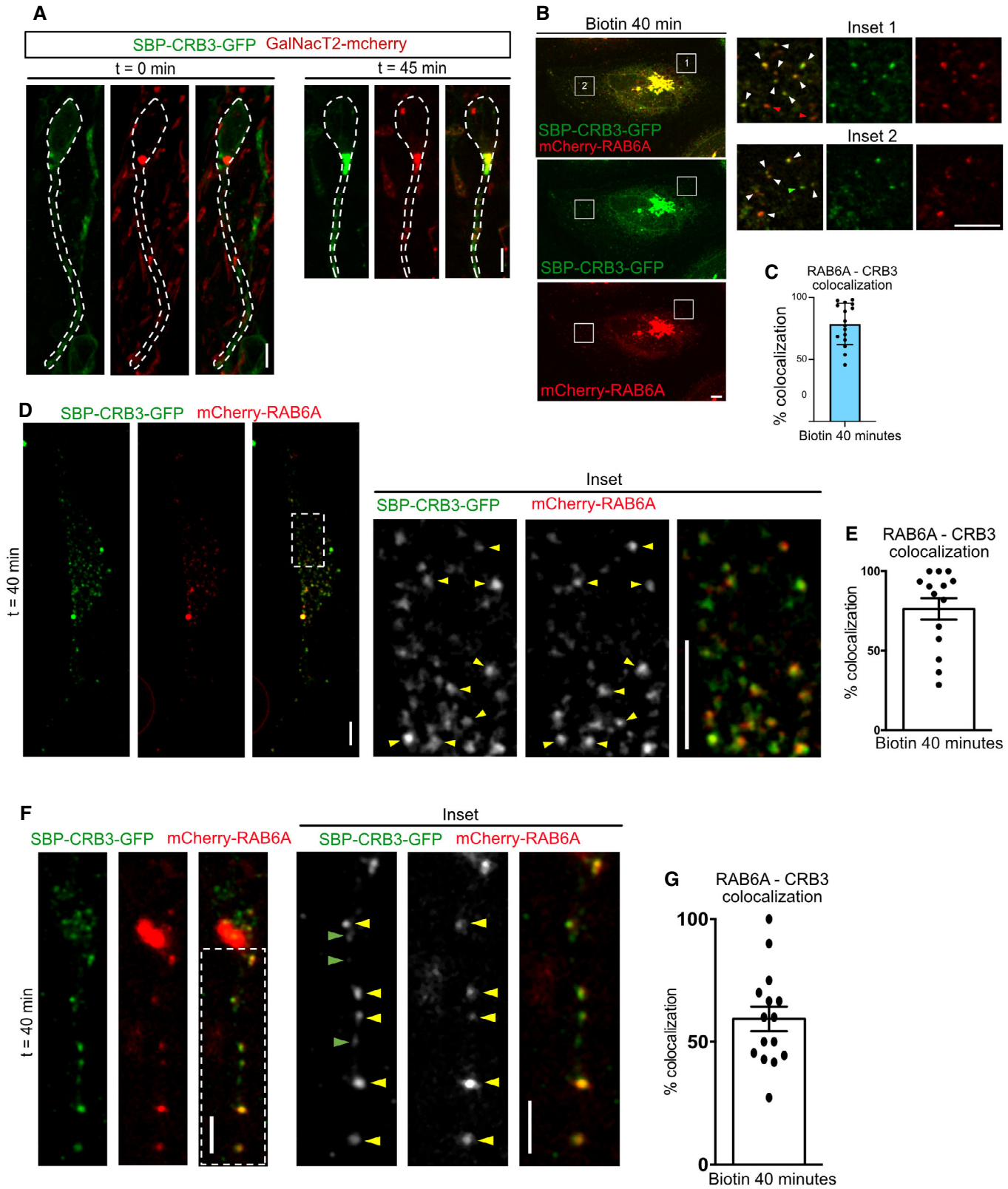
A
SBP-CRB3-GFP GalNacT2-mcherry
t = 0 min
t = 45 min
B
Biotin 40 min
SBP-CRB3-GFP
mCherry-RAB6A
SBP-CRB3-GFP
mCherry-RAB6A
Inset 1
Inset 2
C
RAB6A - CRB3 colocalization
% colocalization
Biotin 40 minutes
D
SBP-CRB3-GFP mCherry-RAB6A
t = 40 min
Inset
SBP-CRB3-GFP mCherry-RAB6A
E
RAB6A - CRB3 colocalization
% colocalization
Biotin 40 minutes
F
SBP-CRB3-GFP mCherry-RAB6A
Inset
SBP-CRB3-GFP mCherry-RAB6A
t = 40 min
G
RAB6A - CRB3 colocalization
% colocalization
Biotin 40 minutes

Figure EV3.

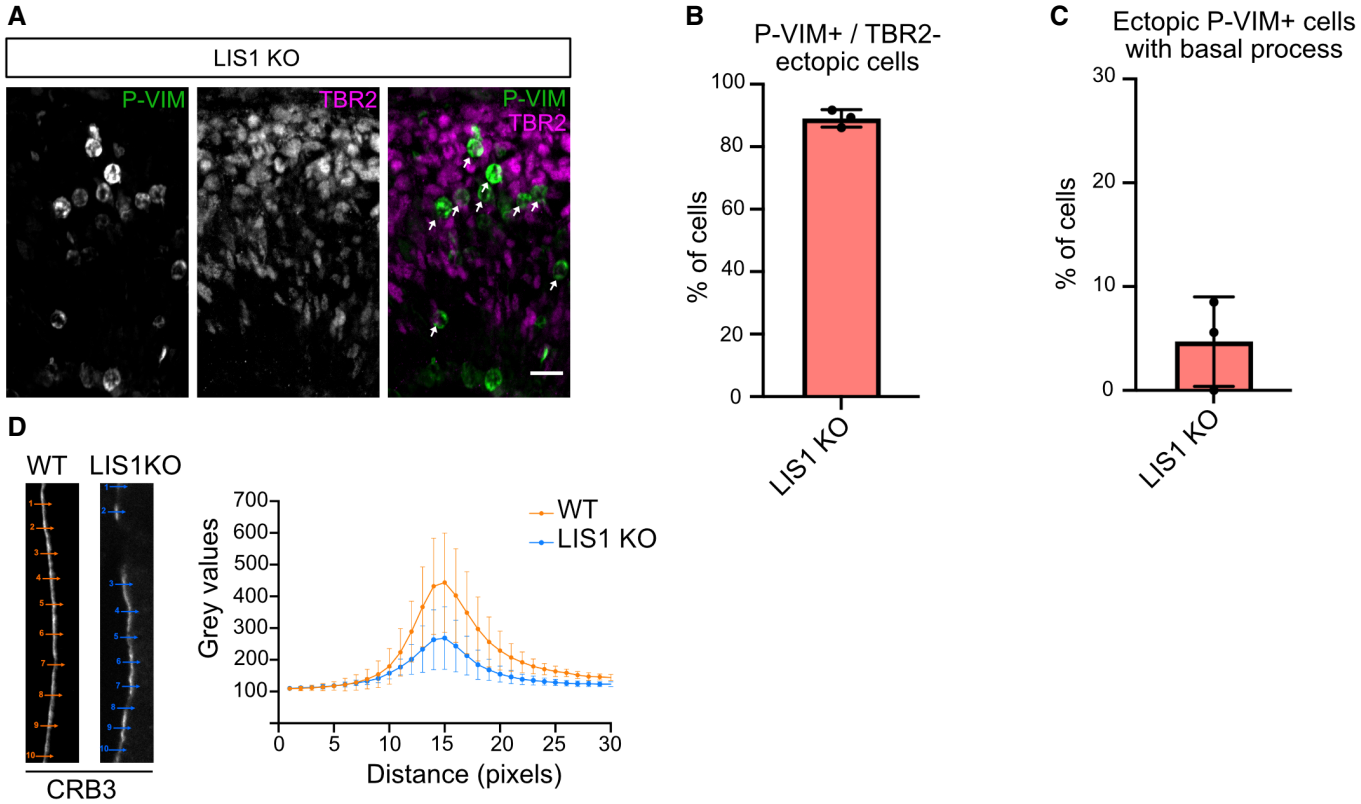

Figure EV4. LIS1 KO leads to ectopic TBR2-negative basal progenitors.

A P-VIM and TBR2 staining in *LIS1 KO* E12.5 brains. Arrows indicate detached P-VIM+/TBR2− cells. Scale bar = 25 μm.

B Percentage of ectopic P-VIM+/TBR2− cells in *LIS1 KO* E12.5 brains. *LIS1 KO*: 301 cells from $N = 3$ brains. Error bars indicate SD.

C Percentage of ectopic P-VIM+ cells that maintained a basal process in *LIS1 KO* E12.5 brains. *LIS1 KO*: 301 cells from $N = 3$ brains. Error bars indicate SD.

D CRB3 average apical signal intensity ± SEM in WT and *LIS1* KO E12.5 brains. $N = 3$ brains per condition.

